# LUMINESCENT CONCENTRATORS BASED ON MONOCRYSTALLINE SOLAR CELLS

BY

JAE HA RYU

THESIS

Submitted in partial fulfillment of the requirements
for the degree of Master of Science in Materials Science and Engineering
in the Graduate College of the
University of Illinois at Urbana-Champaign, 2011

Urbana, Illinois

Adviser:

Professor John A. Rogers

# ABSTRACT

This thesis describes and analyzes various kinds of engineering options for monocrystalline materials for photovoltaics. Monocrystalline semiconductor materials are known for its good electrical performance, but it is not without its drawbacks for its use as solar cells. This thesis explains a little background of solar cells, and describes ways to overcome many of the limitations that conventional solar concentrators fabricated with monocrystalline semiconductor materials have, such as its high cost, mechanical rigidity, heavy weight, opacity, etc. Luminescent solar concentrators (LSC) – a concentrator system that redirects the unused photons through the use of organic dyes – are introduced and new methods for overcoming some limitations of conventional concentrator systems based on lenses and trackers are discussed. Through careful design considerations, an LSC system where more than twice the photons are indirectly collected can be fabricated, and the optics behind the luminescent waveguide is explained.

TABLE OF CONTENTS

CHAPTER 1: INTRODUCTION ..... 1
CHAPTER 2: ULTRA-THIN FLEXIBLE SILICON SOLAR CELLS ..... 3
2.1 Background ..... 3
2.2 Fabrication methods ..... 6
2.3 Results and discussion ..... 9
2.4 Light trapping structures ..... 11
2.5 Figures ..... 14
CHAPTER 3: FLEXIBLE LUMINESCENT SOLAR CONCENTRATORS ..... 26
3.1 Background ..... 26
3.2 Selection of microcells and organic dye ..... 28
3.3 Results ..... 29
3.4 LSC system with GaAs ..... 34
3.5 Figures ..... 38
CHAPTER 4: CONCLUSION ..... 48
REFERENCES ..... 49

# CHAPTER 1

# INTRODUCTION

As many of the dominant energy sources such as fossil fuels are being increasingly scarce, the importance of solar energy is also growing as is a clean and inexhaustible energy source [1]. The solar market has grown significantly over the past few years, and the rate of growth is expected to increase even more rapidly. Many different kinds of photovoltaic cells have been developed and they are separated into multiple categories according to its material, and different types of solar cells display different efficiencies, cost and applications.

Solar cells made by monocrystalline materials are characterized by its excellent performance. The reported values of efficiency for the best performing silicon cell is 25.0% and for gallium arsenide is 28.1%, and these efficiencies exceed the efficiencies of many other materials – multicrystalline Si solar cells have an efficiency of 20.4%, thin film solar cells such as CdTe and CIGS have efficiencies of 16.7% and 19.6% respectively, and for dye-sensitized solar cells (DSSCs) it is 10.9% and organic devices are lower than 10% [2]. As can be seen, monocrystalline Si and GaAs based solar cells are very efficient and outperforms many other existing solar cell materials, but they also have many drawbacks and have many limitations.

One of the major disadvantages of using monocrystalline materials is that it is not cheap – monocrystalline Si is much cheaper compared to GaAs due to its high natural abundance, but compared to poly-Si or other thin-film technologies it is still expensive. Also for silicon, because it is an indirect band gap material, the absorption coefficient for

Si decreases very gradually for longer wavelengths compared to direct band gap materials [3]. So it requires a large quantity of material – typical Si devices are hundreds of microns thick for it to absorb the solar spectrum as fully as possible. So conventionaly Si solar cells are known for its bulkiness – it is mechanically rigid, it is heavy, and requires a lot of material. Because of its rigidness and opacity, it also cannot be used for applications for building integrated photovoltaics (BIPVs) such as solar curtains or power generating windows. Compound semiconductor systems like GaAs, on the other hand, is a direct bandgap material and doesn't require a lot of thickness for it to be efficient, but it is even more expensive than monocrystalline Si. Because of its excellent efficiency, and radiation resistance [3], GaAs based systems have been widely used for space applications.

In Rogers research group a lot of work has been done on monocrystalline photovoltaic systems – even though organics, nanowires, or other new materials hold significant promise, monocrystalline materials still have many opportunities of use, and by finding new methods of exploiting these materials, many of its limitations can be overcome. This paper will introduce some novel ways that allow efficient use of semiconductor materials that will lead to the reduction of cost and new engineering opportunities such as flexible modules and semi-transparent designs while still retaining its good performance, and also discuss flexible luminescent solar concentrators built based on this system for Si and GaAs.

# CHAPTER 2

# ULTRA-THIN FLEXIBLE SILICON SOLAR CELLS

## 2.1. Background

The excellent performance and reliability, and high natural abundance made monocrystalline Si a very widely used and promising material for the future. As mentioned earlier, however, there are many drawbacks associated with conventional Si photovoltaics – it is rigid, heavy, and it is still expensive compared to other thin-film technologies. This chapter will introduce a method of using monocrystalline Si in a way that yields large-scale arrays of micro scale silicon solar cells (μ-cells) from a single wafer. Modules made from these microcells have the good performance characteristic of a monocrystalline photovoltaic cell, and at the same time it can be flexible, light-weight, and have user defined semi-transparency. Before describing these designs the basic operation and design principles will be discussed.

### 2.1.1 Solar cell operation

The basic operation of a solar cell starts with the photon hitting the cell. When the cell is illuminated with photons with energy $E = h\nu$ greater than $E_g$, the band gap of a material, the photon is absorbed and causes electron-hole pairs (EHPs) to be generated. The minority carriers are then collected by the p-n junction to generate current – the p-n junction prevents recombination of these carriers as they are swept across the junction by the electric field at the junction, where it becomes a majority carrier. So in the case where the emitter (top layer of PV cell) is n-type and the base (bulk material) is p-type, the hole

(minority carrier in emitter) is swept across the junction and into the base, where it is now a majority carrier. So in a short circuit condition, the hole travels through the base, and the electron passes through an external load and eventually it meets a hole through the rear contact, completing the circuit. The current in a short-circuit condition is defined as the short-circuit current ($I_{sc}$). In an open-circuit condition where there are no paths for carriers to leave as in the short circuit case, more majority carriers are formed on both the emitter and the base, and this creates a charge imbalance which generates a voltage across the junction, which is defined as the open-circuit voltage ($V_{oc}$). This current and voltage described can generate power.

Some important parameters that define solar cell performance is the efficiency (η) and the fill factor (FF) – the higher these two values are, the better the cell performs. The efficiency is basically the ratio of power generated to electricity over the input power:

$$\eta = \frac{P_{max}}{P_{in}},$$

where $P_{max}$ is the maximum power point and $P_{in}$ is the incident light power. The fill factor is the measure of the squareness of the I-V curve and is defined as,

$$FF = \frac{P_{max}}{I_{sc}V_{oc}},$$

which can be simplified [4] to be related to $V_{oc}$:

$$FF = \frac{V_{oc} - \ln(V_{oc} + 0.72)}{V_{oc} + 1}.$$

So it can be seen that the performance of a solar cell depend strongly on $V_{oc}$, and $V_{oc}$ is also related to $I_{sc}$ as described in this formula:

$$V_{oc} = \frac{nkT}{q} \ln\left(\frac{I_L}{I_D} + 1\right),$$

Where $I_L$ is the light generated current (which is equal to $I_{sc}$ for most cases), and $I_D$ is the dark current of the diode. $I_{sc}$ depends on several factors, such as the area of the solar cell, incident light intensity, and optical properties of the cell.

### 2.1.2 Design principles

In order to ensure maximum performance, certain techniques and principles are implemented in the design of the solar cell. As described earlier, a semiconductor solar cell is a p-n junction. The emitter, usually n-type (has better surface quality compared to p-type), is doped in a way such that i) the emitter thickness is thin to ensure there are minimal losses from minority carrier recombination and ii) the emitter is doped sufficiently to minimize resistance. The base has to have enough thickness to ensure absorption of light – as mentioned in the previous chapter Si and GaAs has indirect and direct bandgaps, respectively, which gives them different thickness requirements.

Anti-reflection coatings with specific thickness

$$t = \frac{\lambda}{4n_1},$$

where $\lambda$ is the chosen wavelength and $n_1$is the refractive index of the dielectric material, and refractive index

$$n_1 = \sqrt{n_0 n_2},$$

where $n_0$ and $n_2$ is the refractive index of air and semiconductor material, respectively, can be used so that the reflected wave at each interface interferes destructively to reduce the reflection.

To increase the path length of the photons, back side reflectors (BSR) can be used. As described earlier, GaAs systems absorb light with a very thin layer and will have

relatively small effects. With Si, however, especially when there thin layers of Si is used, the BSR can help by boosting the absorption significantly. By using a diffuse reflector which randomizes reflected light, the optical path length can be increased by a factor of $4n^2$[5].

Methods for reducing surface recombination is also used a lot, as recombination losses have a significant impact on $I_{sc}$ and $V_{oc}$. One of these methods is to use a back surface field (BSF), which minimizes recombination on the back surface. A BSF is a highly doped region on the bottom of the cell – it is doped higher than the base and the interface between the base and the BSR acts as a barrier for the minority carrier to move to the rear surface [6].

## 2.2. Fabrication methods

### 2.2.1 Ribbon/Mesh Formation

We use a p-type Czochralski Si (111) wafer with a diameter of 3 inches, thickness of 375 µm, and resistivity of 10-20 Ω cm. The wafer is first cleaned with a piranha solution ($H_2SO_4$:$H_2O_2$ = 3:1 by volume) and then followed by an oxide strip using buffered oxide etchant (6:1). It is coated with a layer of $SiO_2$ by plasma-enhanced chemical vapor deposition (PECVD), and then coated with a layer of photoresist (AZ5214). By doing a photolithography step using a contact lithography tool, the shape of the Si ribbons is defined. The oxide layer that is not covered by the photoresist is removed with buffered oxide etchant (~1 min). The resist acts as a mask for the subsequent inductively coupled plasma reactive-ion etching (ICP RIE) which forms trenches that are around 15-20 µms deep. The photoresist is removed with acetone and thoroughly cleaned once again using

RCA1 ($H_2O$:$NH_4OH$:$H_2O_2$ = 6:1:1 by volume, 10 min), the side walls of the trenches are smoothed out by potassium hydroxide (75 ℃, 1 min). The oxide layer is then stripped using hydrofluoric acid (49%).

### 2.2.2 Junction Formation

Once the ribbon structure is formed, the top contacts are doped. A thick layer of $SiO_2$ is deposited using PECVD to serve as a diffusion mask, and then through photolithography (photoresist, AZ4620) the doping windows are opened. A thick photoresist is used in this step to cover the trenches that are deeper than 15 μm. It goes through a similar photolithography step followed by a BOE etching which opens the windows for doping. Solid-state sources of boron (BN-1250) and phosphorus (PH-1000N) were used to dope both p+ and n+ regions, respectively. Boron doping was conducted first at 1000 ℃ under $N_2$ atmosphere for 30 minutes, and then once the sample went through cleaning procedures and photolithography to open the phosphorus window the same way as before, phosphorus doping is conducted under the same conditions but for 10 minutes – as mentioned earlier the emitter (n-type) ideally should be thin, so it is doped for a much shorter period of time. The cleaning procedure used was an HF oxide strip (~1min) followed by piranha and RCA1 cleaning.

Once the top contacts for both p+ and n+ are created, a thin layer of $SiO_2$ and $Si_3N_4$ is deposited using PECVD. A chromium (80 Å) and gold (800 Å) layer is evaporated so that the top surface and sidewalls are covered while region in between the trenches are still exposed – the region in between the trenches is 26μms wide and the trenches are 15μms deep, and tan(30°) = 0.577 = 15/26, so a ±30 degree stage had to be used to create a

shadow in between the trenches. The gold layer acts as an etch mask for the RIE, and the unprotected $Si_3N_4$ and $SiO_2$ layer is etched by RIE using a mixture of $CHF_3$ and $O_2$, and the cells are now ready to go through an undercut procedure. KOH anisotropic etching (preferential <110> etch – etches in the <110> direction much faster than in <111> direction because the bonds it has to break is different from plane to plane) is performed (100 ℃, ~30 min) which forms free standing cells. The metal layers are removed using subsequent steps of Au etchant and Cr etchant, cleaned using piranha and the device goes through another phosphorous doping at the exposed bottom surfaces which forms a back-surface field and yields a fully functional Si photovoltaic cell in a form of ultra-thin ribbons [7]. These fabrication steps are summarized in Figure 1.

### 2.2.3 Transfer printing and Interconnections

After the KOH undercut and the backside doping, the cells are ready for printing. The cells are picked up using a flat elastomeric stamp of polydimethylsiloxane (PDMS). The cells are selectively retrieved by the controlled fracture at the anchors, and the picked-up cells are then transferred on to a different substrate (glass or plastic), using an ultraviolet-curable polymer (NOA61) as both an adhesive and a planarization medium. The stamp and cells are submerged into the NOA layer (~30 μm), they are UV-cured, and the stamp is peeled off. Once the transfer printing is complete, metal interconnects are formed – a layer of gold is sputtered and then it is lithographically defined by using an etch-back procedure, and finally the device is complete. The final module layout is shown in Figure 2.

## 2.3 Results and discussion

### 2.3.1 Demonstration of multiple iterations from single wafer

The fabrication method introduced earlier provides a way for very thin layers of Si ribbons (15~20 μms) to be taken from bulk Si wafers and transfer printed onto foreign substrates. We used a 375 μm thick wafer so after transfer printing a thin layer of Si ribbons several more iterations could be done. After all of the cells are retrieved, chemical re-polishing of the source wafer can be done in KOH to remove the remaining structures and residual doped areas, and then the re-polished wafers can be used for another round of cell fabrication. The bulk wafer could be reused until it is completely consumed, and it has been demonstrated for three times as shown in Figure 3.

### 2.3.2 Cell performance

The performance of these Si microbars is less than the state of the art monocrystalline solar cells, but the fact that no additional methods for improving the cell performance (such as anti-reflection coatings and surface texturization) were implemented should be taken to consideration. I–V measurements of the cells were made in the dark and also in a simulated AM 1.5 illumination condition at room temperature. Figure 4 shows I–V curves of a representative cell with and without a diffuse BSR under AM 1.5 illumination. Without a back side reflector (BSR), this cell has a Jsc of 23.6mAcm$^{-2}$, a $V_{oc}$ of 503mV, a fill factor of 0.61 and an efficiency of 7.2%. The cells are about 15-20μms thick, which is approximately ten times less than the thickness used in conventional systems. In this ultrathin regime, the absorption length of monocrystalline Si for the visible and infrared wavelengths is greater than or comparable to t [8,9]. So by adding a BSR, the

performance can be significantly improved. The top curve in Fig. 3 shows the effects of a diffuse white BSR, where $J_{sc}$ and N increase to 33.6mAcm$^{-2}$ (~42% increase) and 11.6% (61% increase), respectively.

High-levels of mechanical flexibility can be also achieved in this system – an image of a bent module is shown in Figure 5a. By encapsulating the module with a layer of polyurethane (PU, ~30μms) the maximum strains on the silicon and the metal interconnect, which is the most brittle material of the system, are less than 0.3% even with a bending radii less than 5mm. Finite element modeling (FEM) results in Figure 5b confirms these results. The I-V curve in Figure 6a and b shows that the performance is unaffected by bending, and in Figure 6c it shows that fatigue tests for bending up to 200 cycles show little change in performance.

2.3.3 User-definable semi-transparency

Another feature of the fabrication processes shown here is its ability to achieve definable levels of optical transparency, which can be valuable for applications in BIPVs such as power generating windows or solar curtains. This can be achieved by using sparse arrays, which can be defined by etching procedures or step-and-repeat printing. Figure 7a shows a piece of paper with printed text and logos seen through the cells of different inter-cell spacing to demonstrate the effect. Figure 7b shows the transmission spectra of cell spacings ranging from 170 to 26 μm which has areal coverages from 20% to 60% and corresponds to levels of transparency from 70% to 35%.

## 2.4 Light trapping structures

### 2.4.1 Background and Fabrication

Using even less amounts of Si is interesting not only because of its cost, it also provides increased bendability, reduced weight, and improved radiation resistance. But when the microcells (~15µms) are thinned down even more below 10µms, the cell performance drops drastically due to incomplete optical absorption [10]. When light trapping structures are used, however, good energy conversion efficiencies can be used even with less material. Nanostructures of relief on the silicon microcell can be used as light trapping structures which enhance absorption by increasing the optical path length by diffraction, trapping higher order diffracted light by total internal reflection (TIR), and by reducing the reflection. These nanostructures can be formed on top of the microcells as can be seen in Figure 8 – through soft nanoimprint lithography periodic structures can be molded onto an epoxy layer (SU8), and through controlled reactive ion etching with oxygen, the residual material at the base of the recessed features can be removed. The remaining layer serves as an etch mask for another ICP RIE step (using $SF_6$, $C_4F_8$, $O_2$) that etches the exposed region of Si. Then, the remaining polymer is removed by piranha solution (3:1 mixture of $H_2SO_4$ and $H_2O_2$).

### 2.4.2 Results and Discussion

These LTS structures are selected to minimize reflections and maximize diffraction such that there are orders of steep enough angles for a TIR condition. The LTS of silicon posts were chosen to have periodicity, relief depth, and post diameter of 500 nm, 130nm, and 350nm, respectively. Figure 9 shows measured transmission, reflection, and absorption

spectra for functional microcells (~ 6 μm thickness), consisting of bare silicon, silicon with a single layer ARC (80 nm SiO2), with an LTS (P of 500 nm), and with both an LTS and an ARC (LTS+ARC). As shown in Figure 9a, microcells with an LTS and ARC have significantly reduced reflection compared to bare silicon – it provides the lowest reflection throughout the spectral range. Figure 9b indicates that the ARC case has the highest transmission, as might be expected, and the LTS and LTS+ARC case also lower transmission compared to bare silicon, as they increase the optical path length via diffraction and trapping. Figure 9c shows the absorption (100% − R − T) spectra for these same cells, and it tells us that the cases of bare silicon and LTS+ARC show the lowest and highest absorption, respectively – the absorption integrated over 450 to 1000 nm and weighted by the solar radiation spectrum (AM 1.5D) for LTS+ARC, LTS, ARC, and bare silicon are 84%, 83%, 56%, and 45%, respectively.

In order to further optimize the LTS geometry, RCWA and FDTD simulations were done, which shows the absorption of normally incident solar radiation as a function of LTS periodicities, shown in Figure 10a. Several cases were considered – bare silicon absorbs approximately 45% of the solar radiation, with the addition of an ARC (SiO2 80 nm) it is increased to 62%, and for an ideal case where the reflection is zero, the absorption is 74%. Even in an ideal case, the LTS provided improved absorption for all values of P investigated. The relative improvements of LTS over bare silicon and single layer ARC for P = 300, 400, 500, 600, 700, and 800 nm are 72% and 24%, 83% and 32%, 78% and 28%, 73% and 25%, 68% and 21%, and 67% and 20%, respectively. The LTS+ARC increases the absorption even more – with P = 400 nm absorption is 84%, and the relative improvement over bare silicon and ARC is 88% and 35%, respectively. The calculated

absorption also agrees with that measured from optical spectra (Figure 3). Tables summarizing simulation results can be found in Supporting Information (Table S1). The values of RD and D, for a given P, are also important because they determine the distribution of intensity into the diffraction orders. Figure 10b provides a contour map of the absorption as a function of D (y axis) and RD (x axis), for the case of a 6 μm thick layer of silicon with LTS+ARC and P = 500 nm. As can be seen, the highest values occur between 100 to 200 nm and 200 to 400 nm for RD and D, respectively. The optimal ranges of RDs provide low reflection losses, and optimal ranges of D maximize the distribution of light into diffraction orders.

The improvement in absorption directly translates to the improvement of solar cell performance – the energy conversion efficiency is increased significantly. The improvements that these structures provide are shown in Figure 11. A 6 μm thick cell was used, and the efficiency without any BSR or LTS has an efficiency of 5.2%, and when both LTS and a thin layer (~80 nm) of $SiO_2$ anti-reflection coating was used it boosted up to 9.5%. So even with thinner cell thicknesses, high performance can be achieved by the use of light trapping structures that increase the absorption significantly. Simulation data of the percent improvement in absorption as a function of different solar cell thicknesses is shown in Figure 12. From this data we can tell that for bulk devices the improvement is mainly from antireflection, but as the thickness is scaled down the dominant effect shifts to light trapping. This data also suggest that through the use of light trapping structures, cells can be fabricated in a much more cost-efficient way with less material used,

2.5 Figures

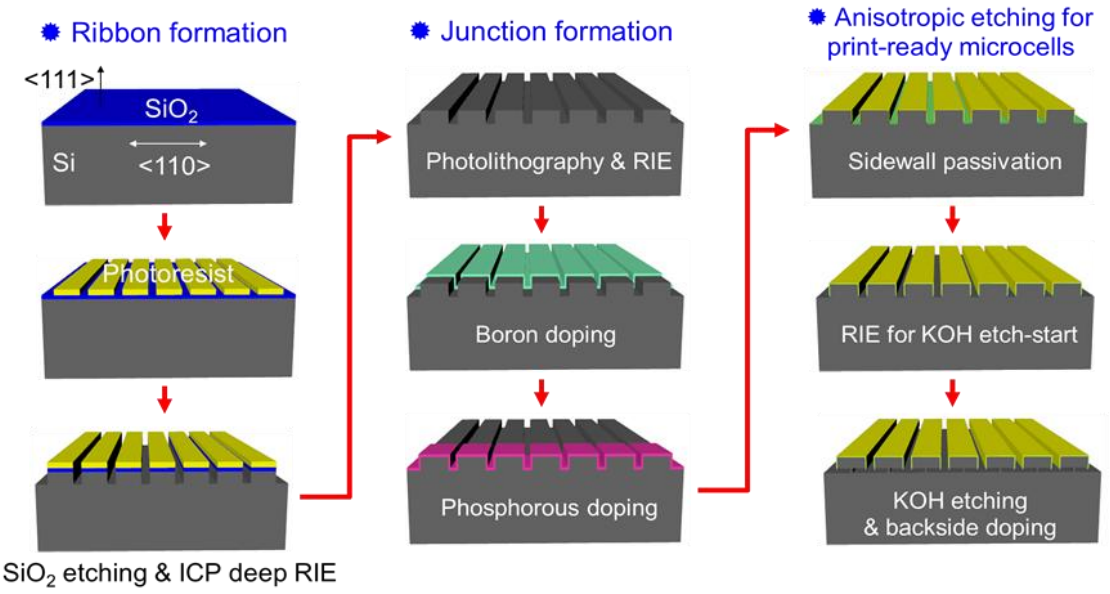



Figure 1. Schematic illustration of the fabrication process for Si microcells. [10]

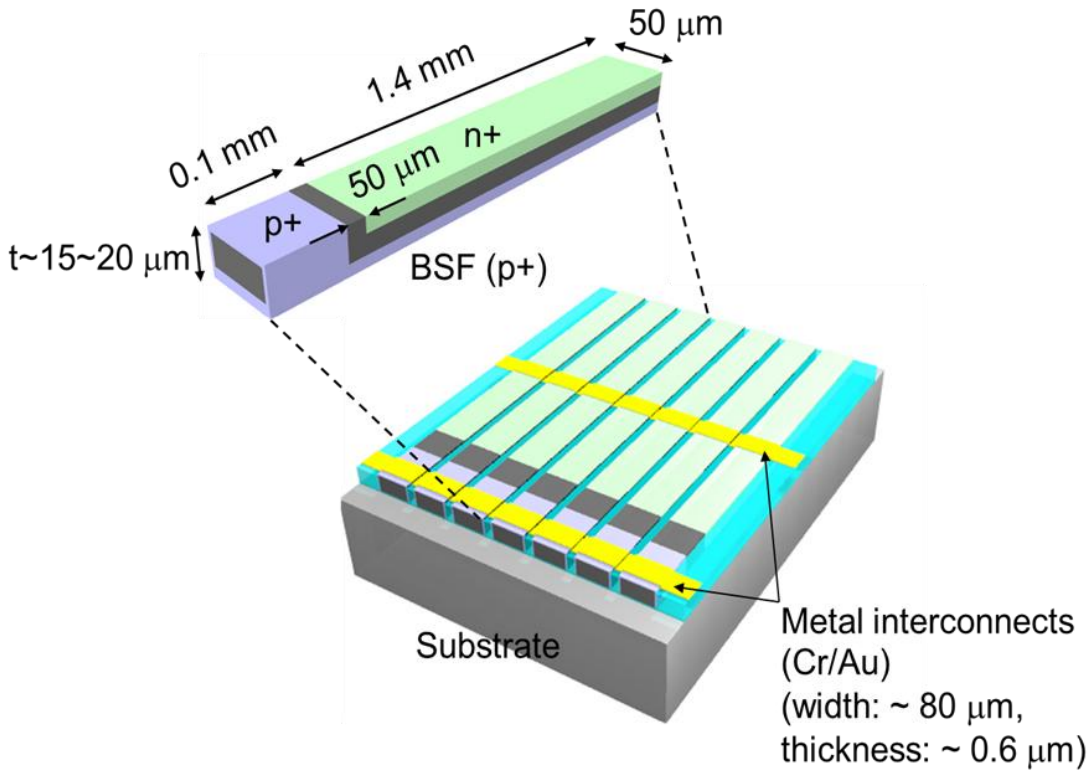



Figure 2. Final cell layout and schematic of the module. The cells have a width of 50 μm, length of 1.55mm, and 15~20 μm thickness. [10]

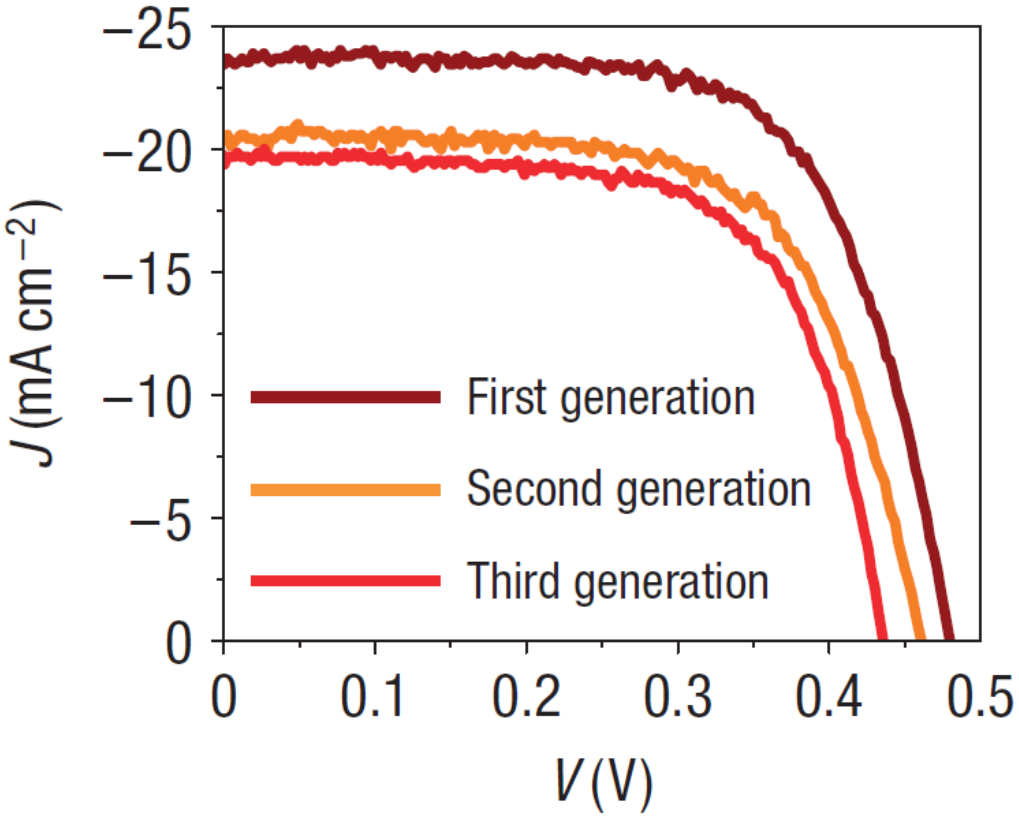



Figure 3. J-V characteristics of a microcell from first, second, and third generation from a single wafer. [10]

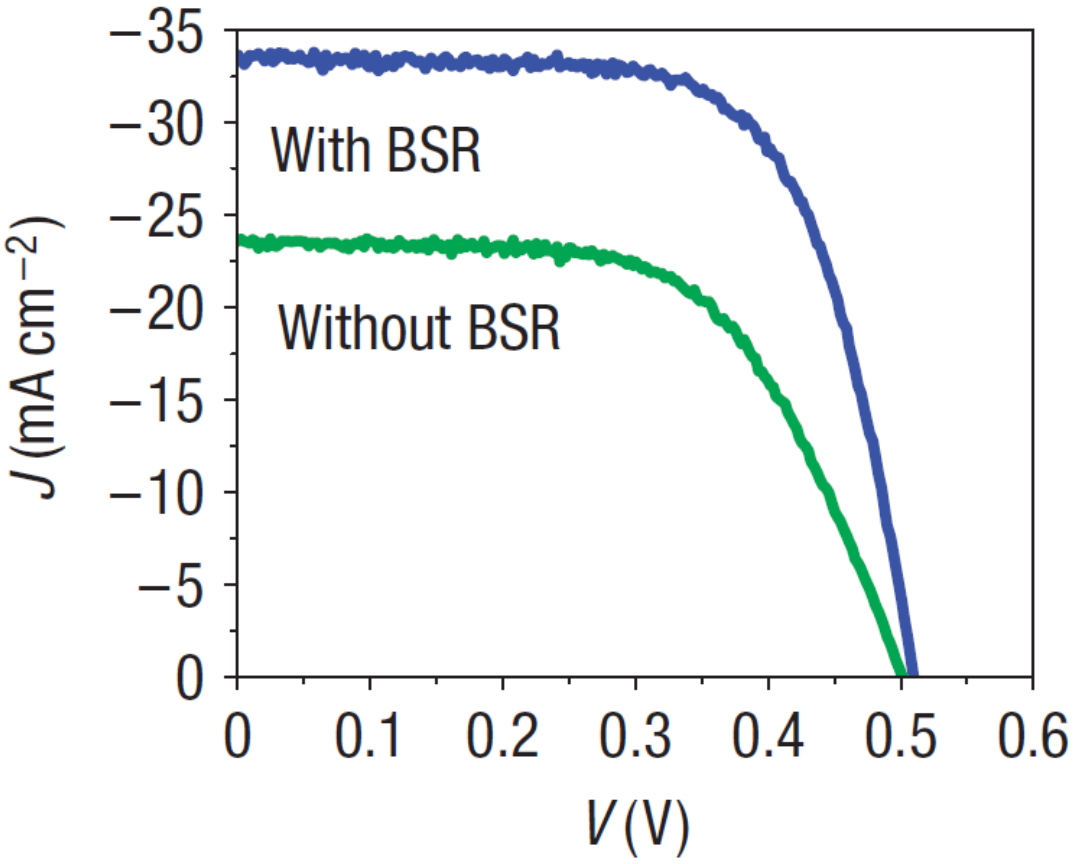
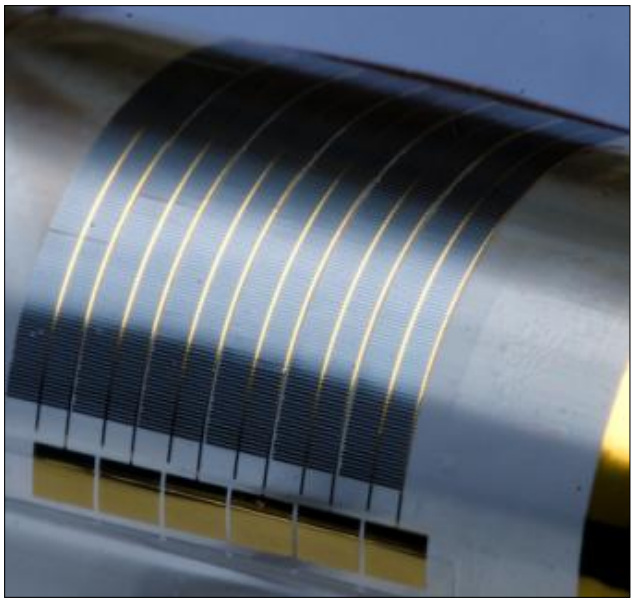



Figure 4. J-V characteristic of a representative cell with and without a back side reflector (diffuse reflector). [10]

(a)



(b)

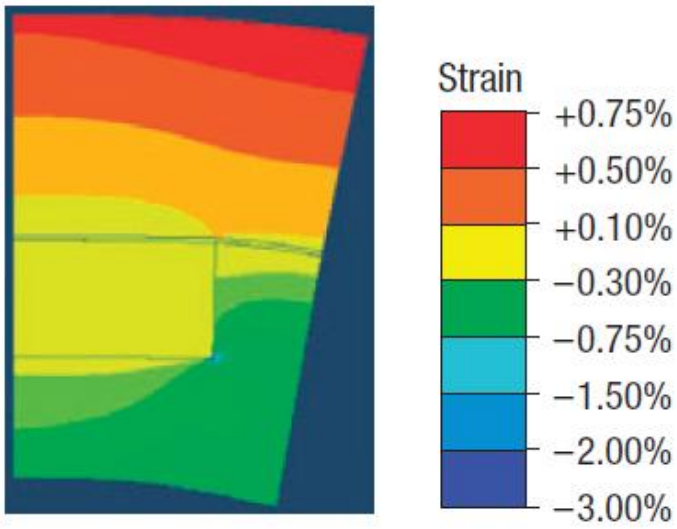



Figure 5. (a) Image of module bent in the direction parallel to the widths of the cells, with bending radius R = 4.9mm. (b) Modeling results of bending strains of module with a bending radius R = 4.9mm. [10]

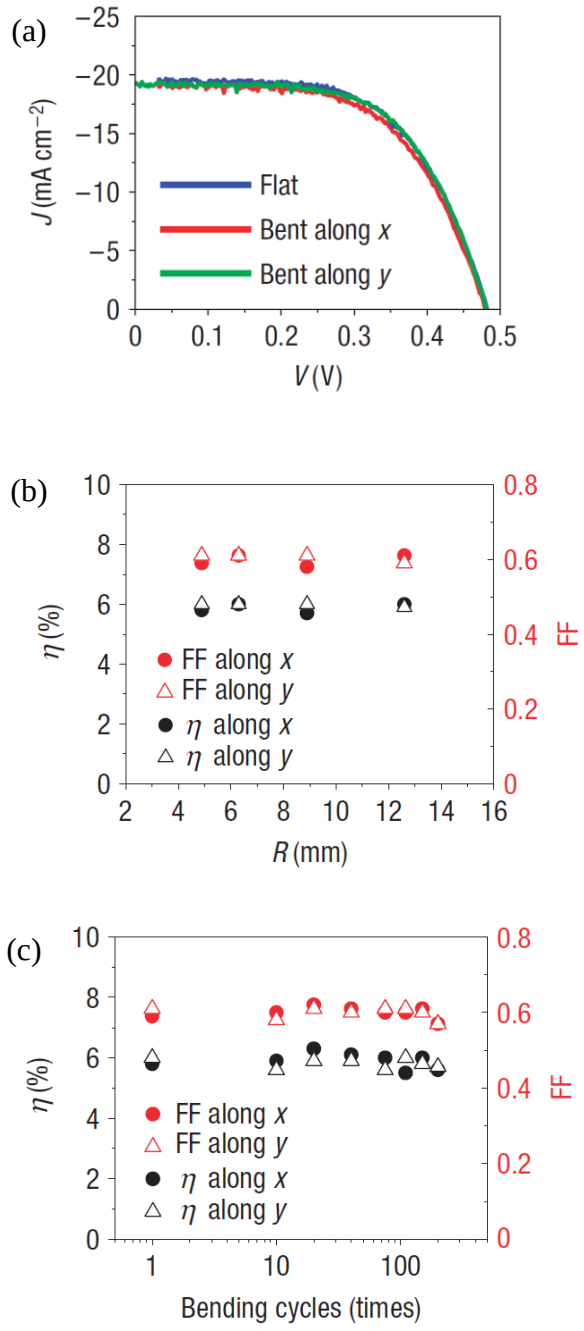



Figure 6. (a) J-V characteristics of a module in its flat state and bent state in x and y directions for R = 4.9mm, (b) Fill factor and efficiency values as a function of radius of curvature, (c) Fill factor and efficiency values as a function of bending cycles. [10]

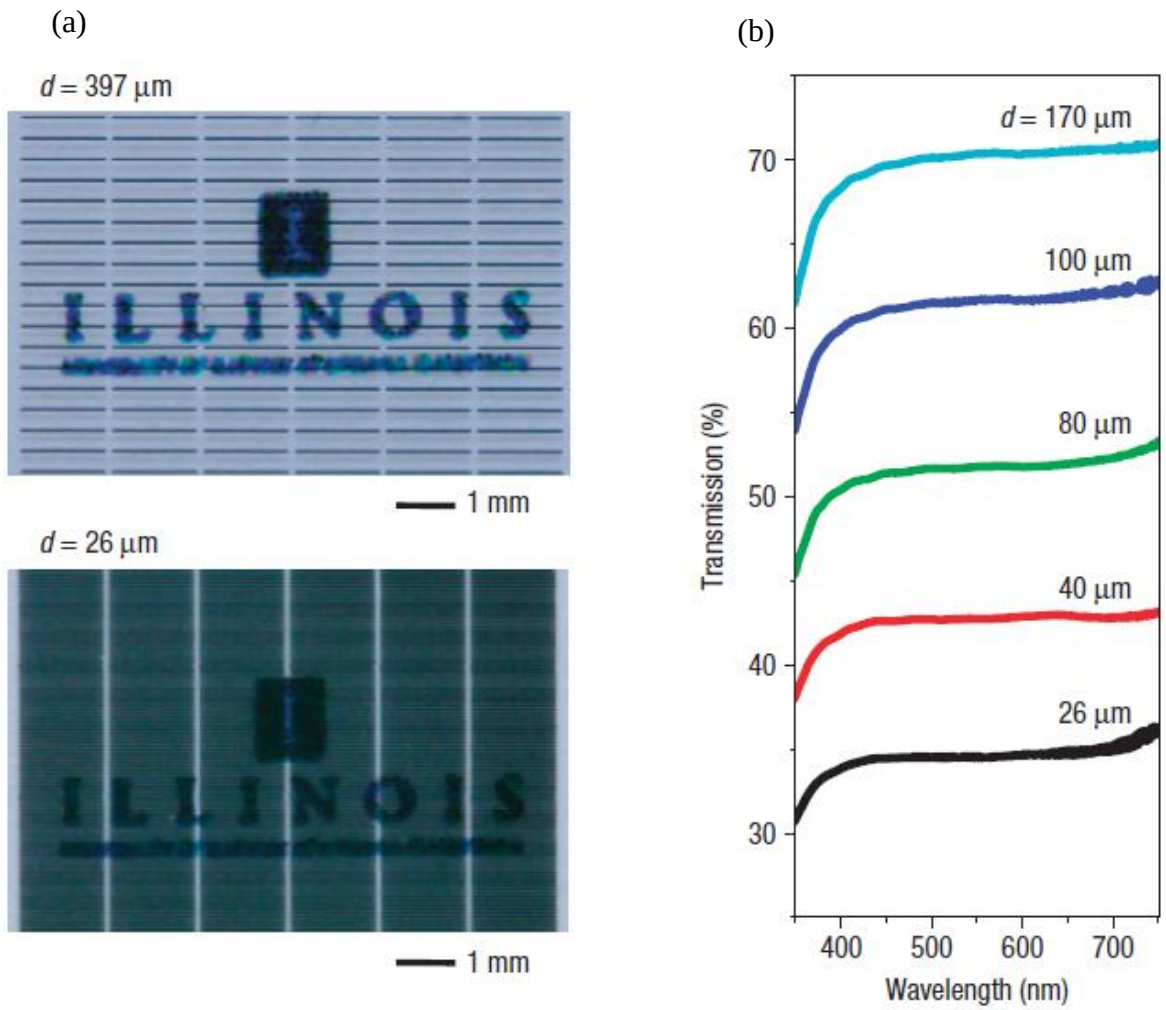



Figure 7. (a) Optical images of text and logo seen through cells with different spacings, (b) Transmission spectra of devices with different spacings. [10]

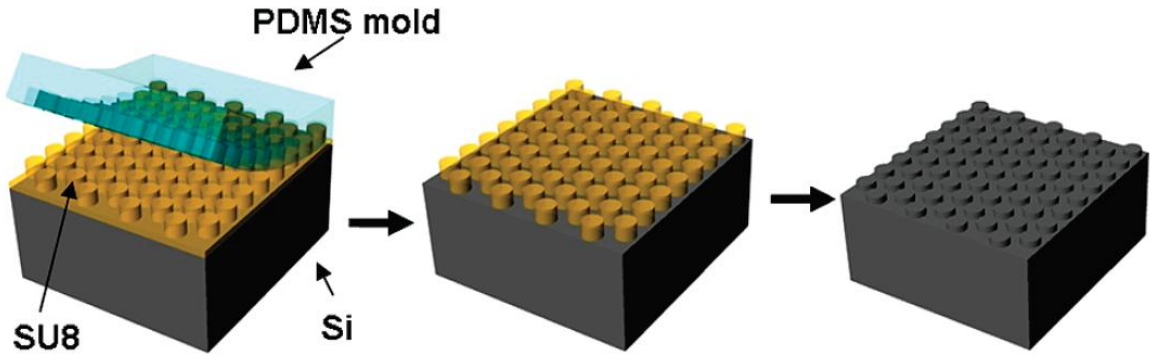



Figure 8. Schematic of soft imprint lithography to form nanostructures of relief. [24]

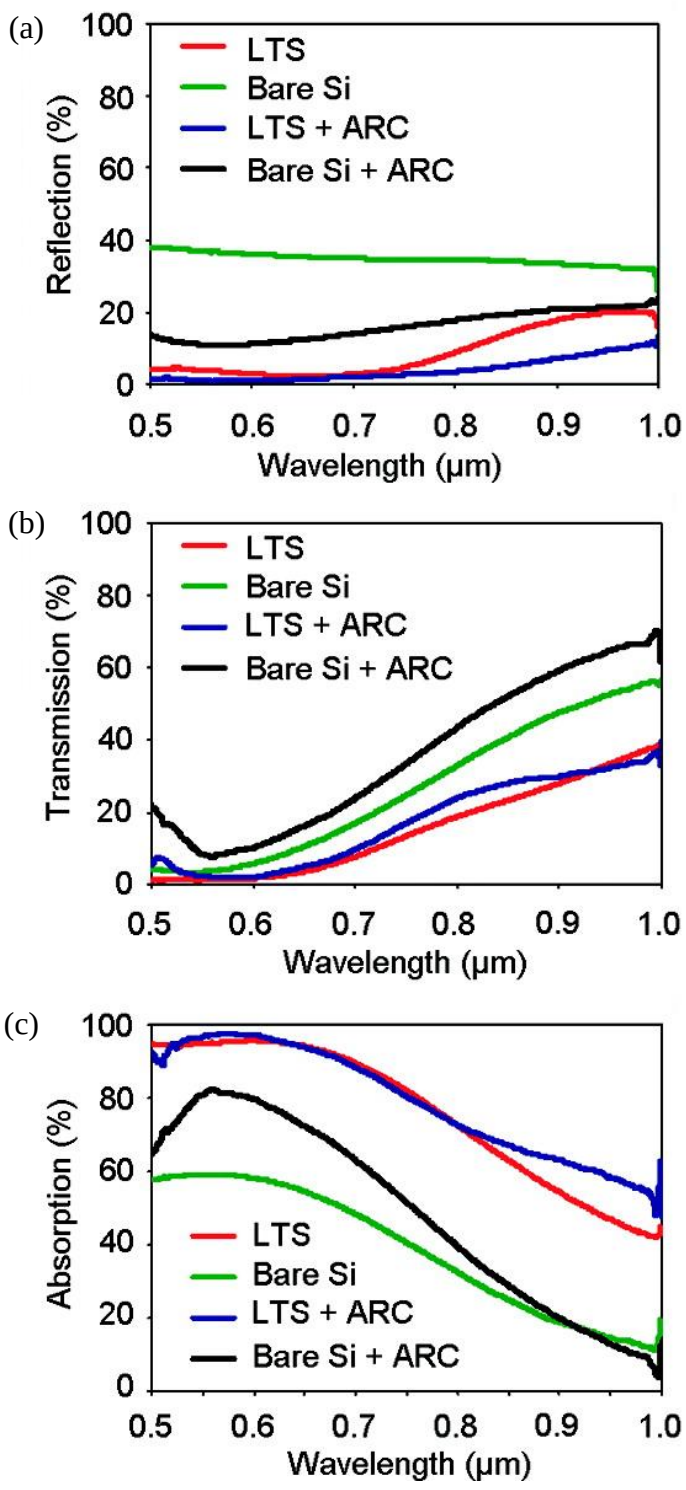



Figure 9. Measured (a) Reflection; (b) Transmission; (c) Absorption of 6 μm thick silicon microcell with LTS, Bare Si, LTS+ARC, Bare Si+ARC structures. [24]

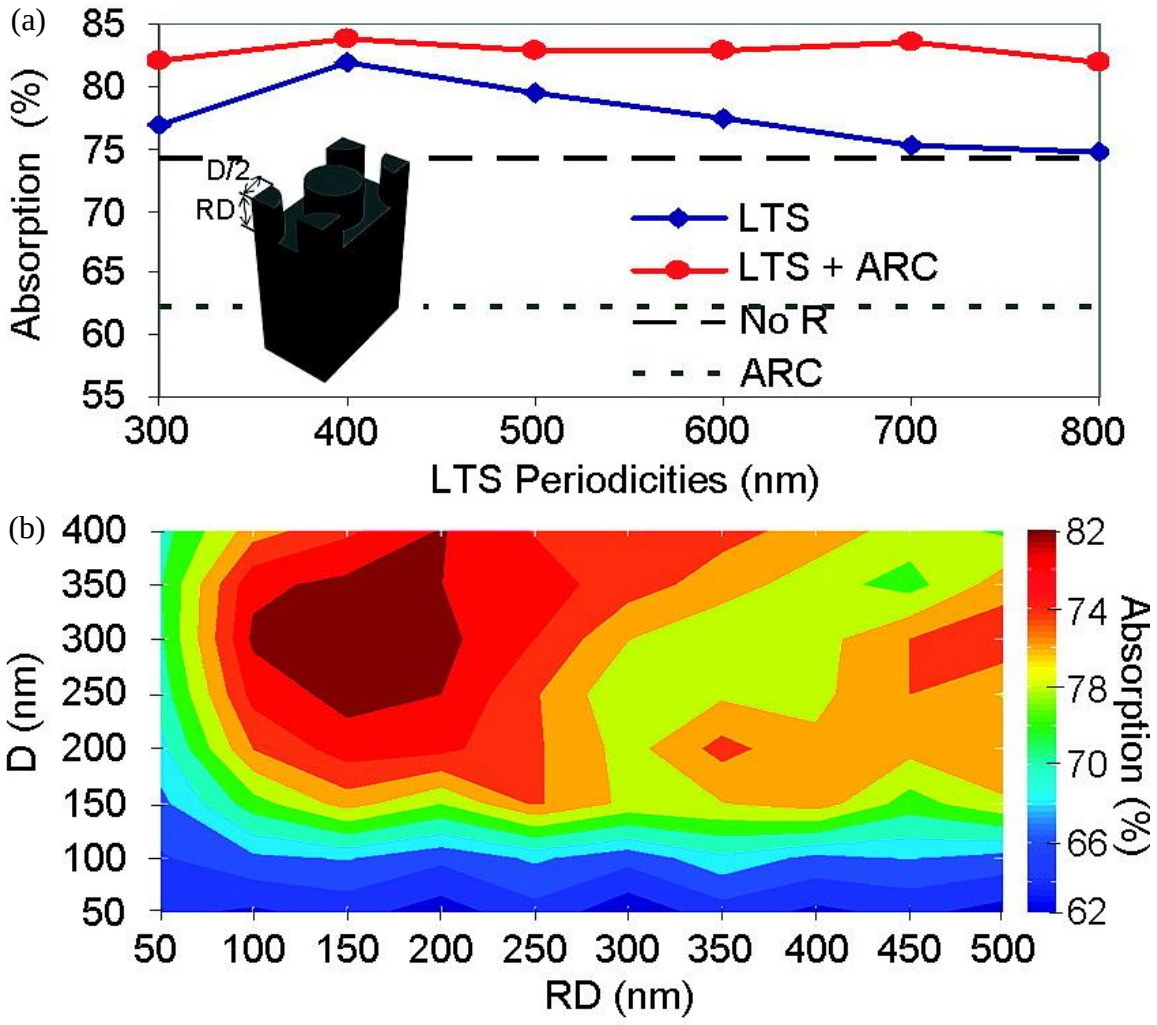



Figure 10. RCWA and FDTD modeling results. (a) Calculated absorption of silicon (6μm thick) with LTS of different periodicities. Bare silicon with no reflection (No R) and bare silicon with ARC (ARC) are included for comparison. (b) Contour map of calculated absorption as a function post diameter (D) and relief depth (RD). [24]

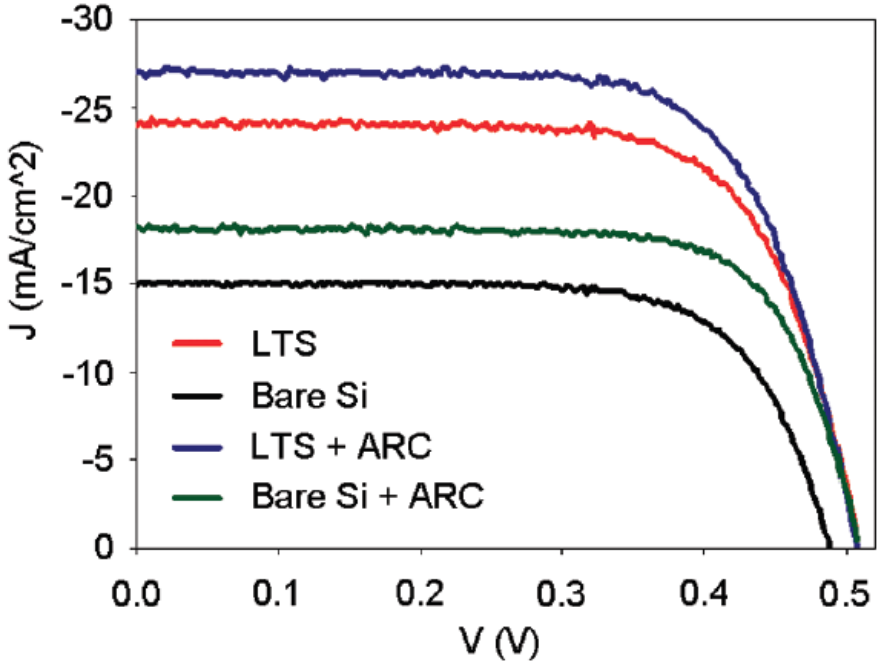



Figure 11. J-V curves of cells without any structure, with ARC, with LTS, LTS+ARC under AM 1.5D illumination. [24]

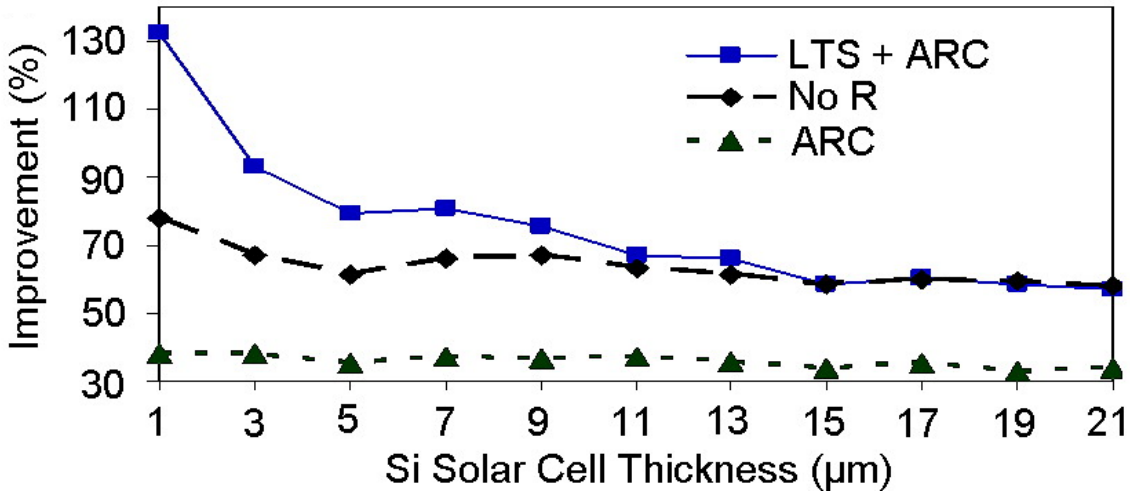



Figure 12. Absorption improvement of silicon with different thicknesses and structures. Perfect ARC case (No R) is included to be compared with LTS+ARC case. [24]

# CHAPTER 3

# FLEXIBLE LUMINESCENT SOLAR CONCENTRATORS

## 3.1 Background

### 3.1.1 Concentrator photovoltaics

Conventional solar concentrators use focusing lenses and mechanical trackers to collect incident solar radiation and redirect it to the photovoltaic cell [11, 12]. Concentrator photovoltaic systems are interesting because the concentration optics can increase their output power while also reducing costs by improving the utilization of the cells. When implemented with high efficiency compound semiconductor PV cells, this concentrator design works great. It has its disadvantages as well – there are challenges in module assembly, complexities involving optics and trackers, difficulties in thermal management and inefficiencies in the capture of diffuse light. Also, these systems do not function effectively in locations where levels of direct normal irradiance are low, and cannot be used in applications that demand mechanically flexible modules because of the bulky components.

### 3.1.2 Luminescent solar concentrators

Luminescent solar concentrators (LSCs) try to avoid these limitations [13, 14, 15]. A simple LSC consists of a planar, multimode slab waveguide doped with a luminescent species. Light is absorbed by the luminescent species, referred to as luminophores, and is re-emitted at longer wavelengths with an isotropic angular distribution. The re-emitted photons that satisfy the TIR conditions at the boundaries of the LSC slab are trapped in

guided modes of the structure. In conventional LSC devices, solar cells are mounted on the edges of an LSC structure to collect emergent radiation. This type of structure is relatively inefficient with direct normal irradiance, but it can concentrate diffuse light effectively, which makes it useful in cloudy days. Also this structure does not require trackers and uses less semiconductor materials, which reduces the complexity and cost.

LSCs have many advantages but it is not without its drawbacks – some of the significant drawbacks of the system include optical inefficiencies from self-absorption, the re-absorption of light emitted by the luminophores, and propagation losses due to scattering and leaky waveguiding [16]. The self-absorption is from the partial overlap of the absorption and emission spectra of the luminophore, and can be reduced with materials that have large Stokes shifts, such as semiconductor quantum dots [17, 18]. The waveguide losses can be decreased by increasing the difference between the refractive index of the LSC material and its surroundings, and also by engineering the structures to avoid scattering. Research is currently being done for pursuing these directions. An important feature of these sources of loss is that their effects diminish with propagation distance. In typical LSC devices, the cells and the LSC waveguides are bulk components. This introduces a restriction for the system – the geometries of key components in the system cannot be used as design parameters for optimizing the behavior, because for bulk components reducing critical dimensions to scales less than several centimeters is impractical. Another restriction is that they cannot be used effectively for mechanically flexible construction, due to difficulties in mounting cells on narrow edges (the thickness range of the LSC should be ~200µms to be flexible) and to increased levels of self-

absorption that result from high luminophore concentrations needed to achieve sufficient optical density in thin layers.

In this chapter an LSC design that overcomes both restrictions is introduced. By using the transfer-printing techniques and ultra-thin silicon solar cells introduced in the previous chapter, arrays of μ-cells can be embedded directly into the LSC waveguide. A key feature is that the dimensions and designs of the μ-cells allow capture of light not only through their top surfaces, but also through their sidewalls and bottom surfaces. Deterministic assembly techniques offer practical access to spacings and array configurations that can match the intrinsic loss characteristics of nearly any type of LSC, even those with extremely small thicknesses (for example, 10 μm or larger), for low-bending stiffness and high degrees of flexibility.

## 3.2 Selection of microcells and organic dye

The solar cell fabrication process is the same as described in the previous chapter. The difference in fabrication is in the transfer-printing step – as can be seen in Figure 13, instead of embedding the cells on a transparent polymer, it is transferred in a layer of dye-doped polymer, which will be referred to as the LSC layer. The cells are embedded in a way that there is unobstructed exposure of their top surfaces to incident light. The organic dye used was DCM, (4-dicyanomethylene-2-methyl-6-p-dimethylaminostyryl-4H-pyran), and the absorption and emission spectra are as shown in Figure 14a. The peak wavelengths for emission and absorption are 602 and 477 nm, respectively. The dye concentration (~0.19 wt%) was chosen such that it provides strong absorption even for thin LSC layers, while at the same time maintains high fluorescence yields as shown in Figure 14b. The

BSR used in the experiments consists of a black anodized aluminium plate, a silver mirror, or a white polyester cloth mounted on the mirror, to provide non-reflective, specular and diffuse reflective conditions, respectively. The measured reflectivities for the specular, diffuse and non-reflective cases are 98, 93 and 22% averaged through the spectral range of 400–1,100 nm, respectively. Figure 15 shows a representative module consisting of sparse arrays of μ-cells printed directly into the DCM LSC layer on a glass substrate.

## 3.3 Results

### 3.3.1 Study of a model luminescent solar concentrator with single cell

To study the optics of the LSC system, a simple model structure is designed. It consists of a single μ-cell implemented in an LSC system with variable illumination area, as shown in Figure 16a. The thickness and width of the cell is same as described earlier – 15 μm and 50 μm respectively. The thickness of the LSC layer is h = 24 μm, and the thickness of the glass slab (h′) is 1mm. Electrical contact pads (30 μm×50 μm, Cr/Au) are defined on the n+ and p+ regions by photolithography and electron beam evaporation. The variable illumination area is implemented by covering the top surface is with a metal (Cr/Au) which blocks incident light and then opening only a certain area of the LSC immediately adjacent to the μ-cell through photolithography.

Figure 16b shows the measured J-V curve under simulated AM 1.5D illumination (same as in the previous chapter) for variable aperture areas (1.6 mm×d μm, where d is the distance between the edges of the μ-cell and the aperture), with a specular reflective BSR. As d increases, the fill factor remains constant and the open-circuit voltage ($V_{oc}$) increases only slightly, while the short-circuit current density ($J_{sc}$) increases significantly. These

trends are all consistent with an increasing total photon flux into the μ-cell. Figure 16c show results of normalized maximum output power ($P_{max}/P_{max,0}$), where $P_{max}$ is the maximum total output power of the cell, and $P_{max,0}$ is the maximum output power when light is incident only through the top surface of the μ-cell (maximum power when d=23μm and a non-reflective BSR). As d increases the region of the LSC increases, and as expected the performance increases with d because with more LSC exposed to light, additional photons are guided to the μ-cell. The rate of increase diminishes with d, however, due to propagation losses, geometric effects and others described subsequently. Measurements on a device with a diffuse BSR but without DCM show that the μ-cell geometry allows effective capture of scattered photons incident on the bottom and sidewall surfaces, even without the LSC mechanism. The normalized maximum output power approach saturation values, $P_{sat}$ (which goes as high as $P_{sat}$ = 1.9 for specular BSR with DCM), at d~ 400 μm=$d_{sat}$. This length scale is well matched with the microscale solar cells described in the earlier chapter, but not with conventional LSC systems.

Figure 16c tells many useful information. For the case where d is close to zero, light captured mainly through the direct illuminated light on the top surface of the cell and from unabsorbed light that reflects from the BSR and enters back through the bottom surface – we can see that the non-reflective case has $P_{max}/P_{max,0}$ ~ 1. The device with diffuse BSR shows $P_{max}/P_{max,0}$ ~ 1.11, and the case without DCM also shows similar behavior as expected because of the small thickness of the LSC material under the μ-cell. The specular case is slightly better with $P_{max}/P_{max,0}$~1.17, as it corresponds to full, double-pass operation. As d increases, the normalized maximum output power improves for all cases because there are increases in photon capture via flux through the sidewalls and

bottoms of the μ-cells, from scattered, reflected and waveguided photons. The non-reflective device shows the smallest $P_{sat}$, because there is no waveguided and reflected photons that contribute as most of it is eliminated by the non-reflective BSR. The diffuse BSR device without DCM shows larger $d_{sat}$, and smaller $P_{max}/P_{max,0}$ compared to devices with BSR because there are no self-absorption losses with no dye. The specular system with DCM shows higher $P_{sat}$ than the case with diffuse BSR because of favorable effects of the specular BSR on waveguiding.

Numerical modeling (done by collaborators in Mechanical Science and Engineering Department, Professor Harley T. Johnson) verifies experimental results, and also provides additional detail. The simulation takes many parameters into account – it includes multiple scattering processes at various interfaces, as well as isotropic emission and self-absorption of the luminophores. The performance of the μ-cells depends on the integrated photon flux, $K_\Phi(d)/K_{\Phi,0}(d)$, where $K_\Phi(d) = \int_{300nm}^{1100nm} \Phi \, d\lambda$, where Φ is the photon flux absorbed by the cell. $K_\Phi(d)/K_{\Phi,0}(d)$ can be compared directly with experimental values of $P_{max}/P_{max,0}$, assuming that the output power increases linearly with absorbed photon flux. The results, presented in Figure 17a, show good agreement with experiment. Discrepancies might arise from experiment conditions, non-ideal waveguide geometries, and surface roughness.

Also, these calculation techniques can be used to optimize the design and to evaluate the influence of different loss mechanisms. There are various kinds of loss mechanisms such as non-TIR losses (incomplete internal reflections of photons that do not satisfy the TIR condition and are lost on the top surface), self-absorption losses (absorption and non-radiative relaxation by the DCM for spectrally resonant photons), BSR losses (due

to absorption), and other parasitic losses from scattering and non-ideal features on structures. Through modeling, the loss mechanisms can be investigated further. Figure 17b shows simulated data of the specular BSR case when each loss mechanism is eliminated (except for parasitic losses which will be neglected). It can be easily seen that the non-TIR loss is the primary loss mechanism – when a lossless BSR and no self-absorption is assumed there is only a slight improvement, whereas when we assume there are no non-TIR loss $K_{\Phi}(d)/K_{\Phi,0}(d)$ at d=600 μm increases to ~2.5.

The thickness of the substrate, h′, also affects the system – as h′ increases, the solid angle subtended by a μ-cell from any point at the BSR surface decreases. So when h′ is much larger than w, the probability that a reflected photon will hit the cell will be close to zero. When h′ decreases to zero, however, the self-absorption and BSR losses will become more significant due to confinement of light in the LSC layer. In particular, for LSC optical densities near unity, the propagation lengths due to re-absorption are comparable with the LSC thicknesses (h) that, by necessity, lie in the sub-mm range for flexible designs. These observations on behavior for limiting cases of thick and thin substrates suggest that there exists an optimal value of h′, where a few hundred microns provide a good balance.

### 3.3.2 Performance of module with arrays of cells

A module-level system is constructed using distributed arrays of μ-cells, with different cell-to-cell spacings (s) are studied. Figure 18a shows a representative device with s=400 μm where the metallic aperture ensures that each module gets constant illumination area. The current-voltage measurements were made near the center of the

array in each case. The measurements on modules with different spacings yield data qualitatively similar to the data from the model experiment as shown in Figure 18b. As demonstrated before, the specular BSR shows better performance than for other cases, and the maximum normalized power intensity is ~320%, which corresponds to a situation where more than twice as many photons are indirectly collected through the sidewalls and bottom surfaces of the μ-cells than those directly incident on the top. The values of $d_{sat}$ for the array cases are smaller than those for model systems, because for the array case there are losses associated with the μ-cells. In the array case there are photon flux from both sides of the μ-cells, which leads to values of ($P_{sat}$−1) that are expected to be, very roughly, two times greater than those for the model system.

### 3.3.3 Mechanically Flexible Designs

This design allows for a mechanically flexible luminescent solar concentrator system. A module of optimized design (s=400 μm, specular BSR), as introduced in the previous section, was made on thin sheets of polyethyleneterephthalate (thickness ~50 μm), and in layouts that implement a top coating of polyurethane (~30 μm) to yield a neutral mechanical plane layout. The polyurethane acts as an ARC – it reduces the reflection losses at the surface of silicon, and also changes other optical characteristics of the structure. Figure 19a shows such a module bent on a cylindrical support. Each row in the array consists of 21 μ-cells interconnected with metal grid lines. The I-V curve in flat and bent states for two different radii of curvature appears in Figure 19b. There are several differences in the design (no glass substrate, BSR is located right below the LSC layer) quantitative comparison against the modules previously described is not straightforward.

The current densities per cell are, however, comparable: ~41 mA $cm^{-2}$ for the specular BSR system (s=400 μm) on a flat system on glass substrate and ~31 mA $cm^{-2}$ for the flexible module, where the flexible interconnected system includes ohmic losses and other adverse effects, including μ-cell variability, that reduce the performance. When the module is bent, there is a decrease in flux associated with reductions in projected area, which causes the output power to decrease slightly. The short circuit currents measured in these bent states decrease to ~83% (R=6.0 mm) and ~74% (R=4.5 mm) of values in the flat state. The corresponding reductions in the projected areas are 87 and 77%.

## 3.4 LSC system with GaAs

Another monocrystalline material, GaAs, is also interesting for many electronic applications, due to its direct bandgap and high electron mobility [19, 20]. GaAs, as a photovoltaic cell, also has advantages in that it has high absorptivity, excellent efficiency, low temperature coefficient, and good radiation resistance [21]. Its main disadvantage is its extremely expensive cost, but researchers came up with a novel method that yields large quantities of high quality materials capable of device integration in large area formats [22] – similar to the Si work, multiple generations of devices can be fabricated just from a single wafer, which give ways to overcome its major disadvantage.

### 3.4.1 GaAs fabrication process

The GaAs bifacial wafer has a p-on-n structure (which was grown using MOCVD by collaborators in the Electrical and Computer Engineering department, Professor Xiuling Li's group), and the thickness of each layer is shown in Figure 20. The summary of the

fabrication steps are shown in Figure 21. In the beginning the wafer is cleaned thoroughly by acetone, IPA, and DI water, and the natural oxide is etched in a mixture of HCl and DI water (1:1 by volume). Then through photolithography, the top contact is patterned and etched using a mixture of citric acid and $H_2O_2$ (4:1 by volume), where the thin $Al_{0.4}Ga_{0.6}As$ layer acts as an etch stop. Once the etching is finished, the wafer is cleaned for another step of photolithography, where the bottom contact is exposed. The bottom contact is exposed by a controlled wet etching of a mixture of $H_3PO_4$, $H_2O_2$, and DI (1:13:12 by volume). Since the bottom contact is extremely thin (300 nm), it is extremely important to control the etching precisely. Once the bottom contact is exposed, the wafer is cleaned and goes through another photolithography step that isolates the cells from each other. The etching is done through a mixture of $H_3PO_4$, $H_2O_2$, and DI again, and is etched all the way down to the sacrificial layer ($Al_{0.95}Ga_{0.05}As$). Once isolation is complete, both top and bottom metal contact pads are formed – through photolithography an opening is created, metal is evaporated using E-beam evaporator, then the PR is liftoff by acetone. For the top contact metal Pt/Ti/Pt/Au (10/40/10/80 nm) is deposited, and for the bottom contact metal Pd/Ge/Au (5/35/80 nm) is deposited, and to form ohmic contacts, it is annealed at 175℃ for an hour in $N_2$ ambient. Once the metal pads are formed, partial etching of the sacrificial layer is done by using diluted HF (HF:DI = 1:20 by volume), and through similar steps of photolithography, holes are formed and etched all the way down to the sacrificial layer by a mixture of $H_3PO_4$, $H_2O_2$, and DI with the same ratios. Then the sample is immersed in diluted HF (1:20, 2.5 hours) for an undercut where the PR acts as a support layer.

Once the undercut is finished, the GaAs cells are picked up using a flat PDMS stamp, similar to the Si process. A clean substrate (glass or thin sheet of plastic) is

prepared, and DCM doped PU is coated. Depending on what LSC structure is required, this step may vary – for multi-layered DCM structures, the PU will be partially cured by UV light before another PU can be coated on top. Similar to the Si case, the stamp is brought to contact to the polymer, UV light cures the PU, and then the stamp is peeled off. The PR is removed using acetone, and then a layer of SU8-2 is spun and via holes for the metal contact pads are formed by photolithography. Then through another photolithography step by using a lift off PR (AZnLOF2070) to define the pattern, and then sputtering a layer of Cr/Au (30/300 nm) on top, the metal interconnects are created. The cell fabrication process is then finalized by encapsulating the sample by SU8-2 and opening the metal pads through photolithography.

### 3.4.2 Experiments with GaAs LSC

Implementing GaAs photovoltaics into the previously described LSC system is also very interesting – GaAs based photovoltaics are often used in a concentrator system due to its good characteristics described earlier, and while conventional concentrator designs are also interesting, a new design involving luminescent dyes are interesting to explore. The data and results shown in this section is work in progress.

The GaAs LSC design is similar to what was used in the Si LSC system described earlier – the cells are sitting on the LSC layer instead of mounted on the side of the LSC structure. The DCM dye used matches GaAs better – the emission wavelength of 0.602μm has an energy E = 1.24/0.602 = 2.06 eV, which is closer to the band gap $E_{g,GaAs}$ = 1.42 eV rather than $E_{g,Si}$ = 1.1 eV. Because the wafer is only few microns thick, in this system there are minimal effects from the photon flux on the sidewalls. To utilize the photons coming

from the bottom, a bifacial cell [23], which can absorb light from the bottom surface, is used. This bifacial cell gives about 1/3 the performance when illuminated from the bottom compared to top illumination. Work on optimizing the dye concentration, thickness, and structure is in progress. Figure 22 shows some preliminary data on various structures. Figure 22a shows an illustration of a multilayered structure where only the top and the bottom layers are doped with DCM while others are undoped – this structure can increase the path length of photons and reduce self-absorption. Figure 22b shows J-V curves of the structures that are labeled, and Figure 22c shows the efficiencies and indirect gain of these systems – the indirect gain is at 3.2, which is comparable to the Si case. Structured BSRs right underneath the LSC layer are also being considered, to reduce self-absorption losses and for efficient capture of light that travels in the waveguide at a very low angle.

3.5 Figures

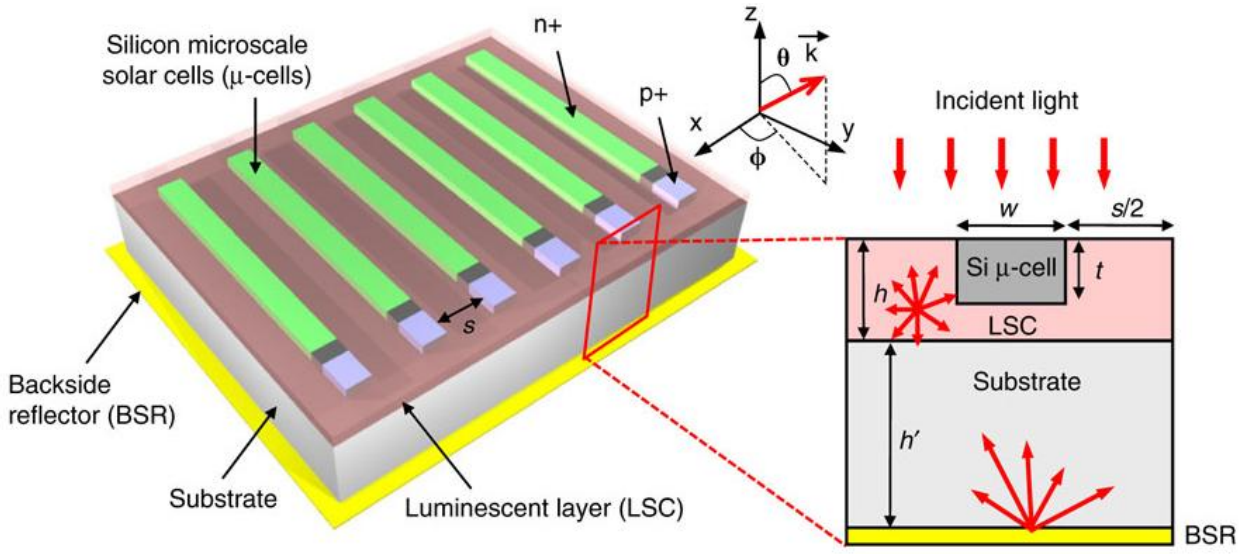



Figure 13. Illustration of the LSC device. The cell dimensions are the same as before with w ~50μm, t ~ 15-20μm. The LSC layer and the glass substrate has thickness of h = 24μm and h' = 1mm, respectively. Various BSRs and cell-to-cell spacings are used. [25]

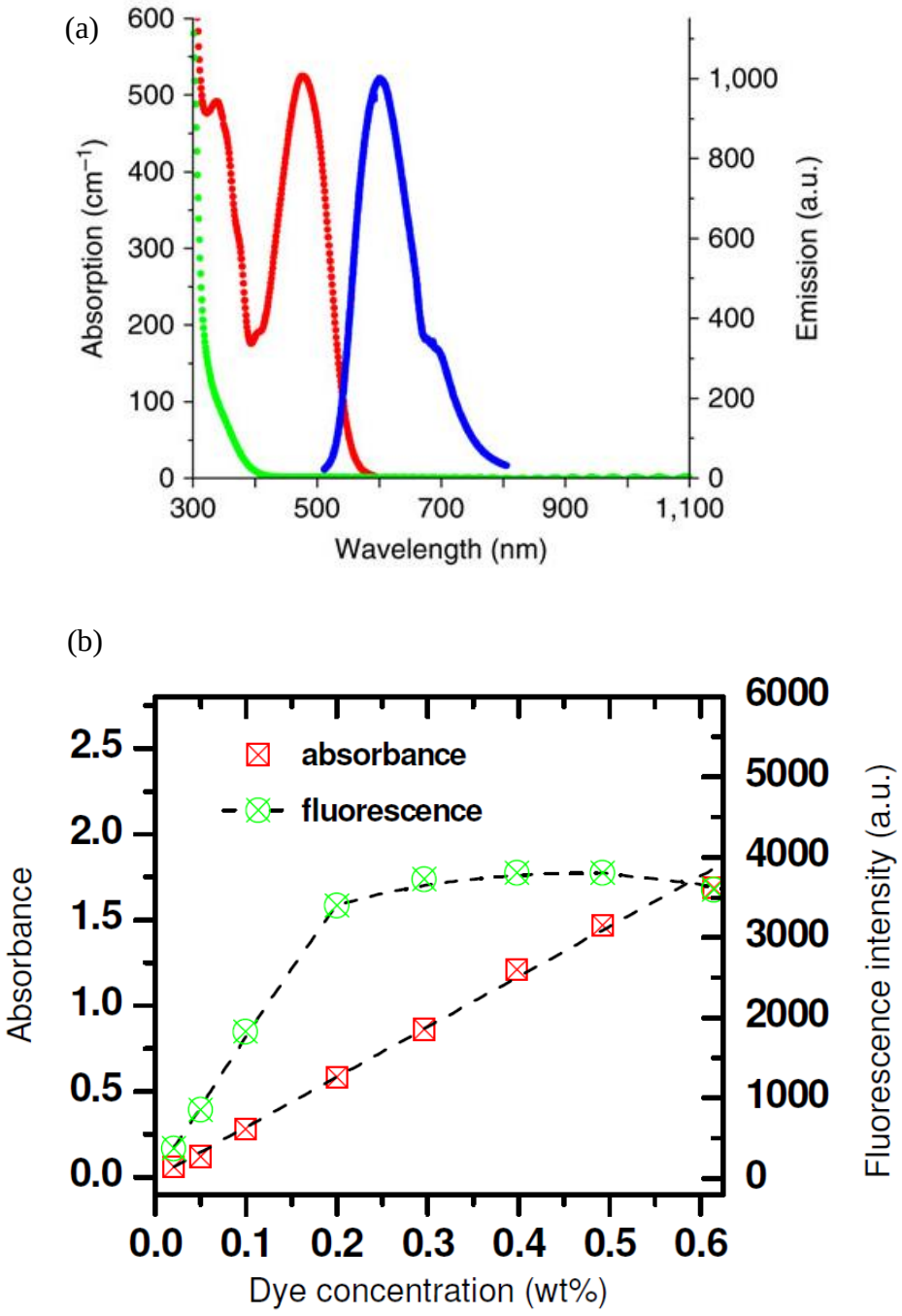



Figure 14. (a) Absorption and emission spectra of DCM dye. (b) Absorbance and fluorescence of DCM dye as a function of dye concentration. [25]

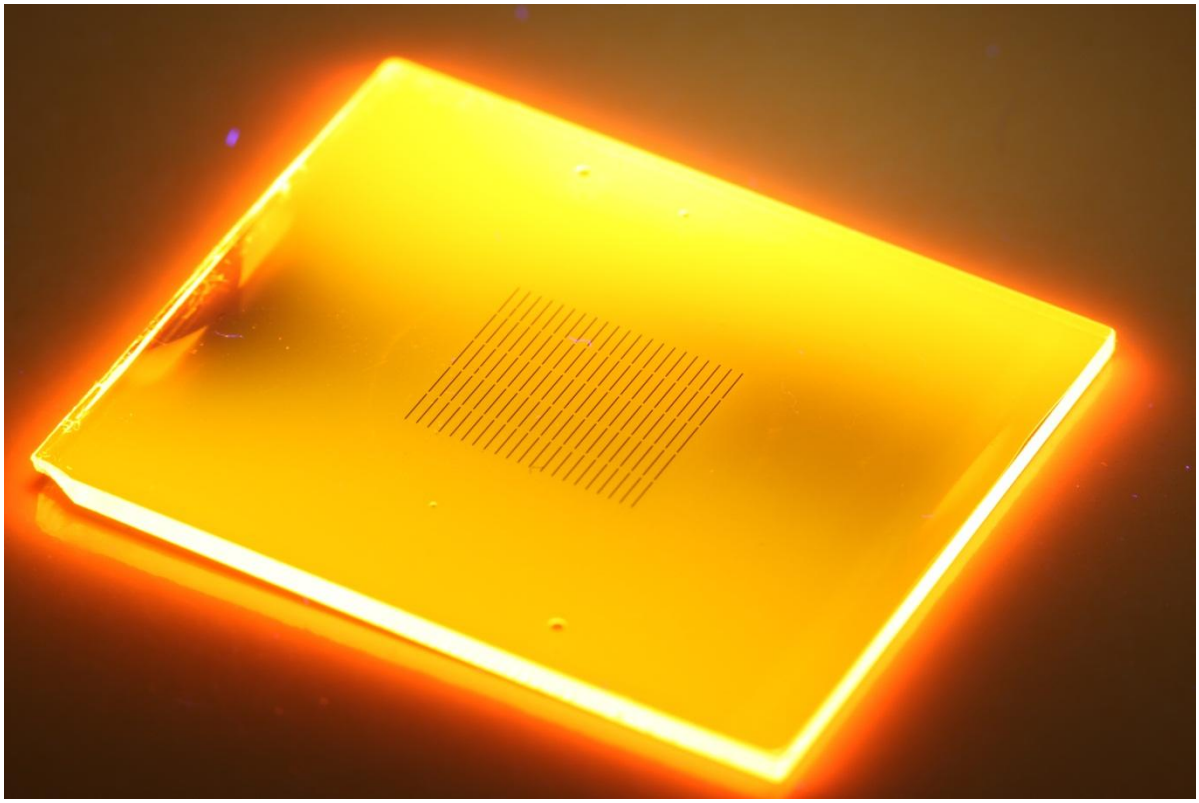


Figure 15. Photo of a completed module before forming interconnects, under UV-illumination. [25]

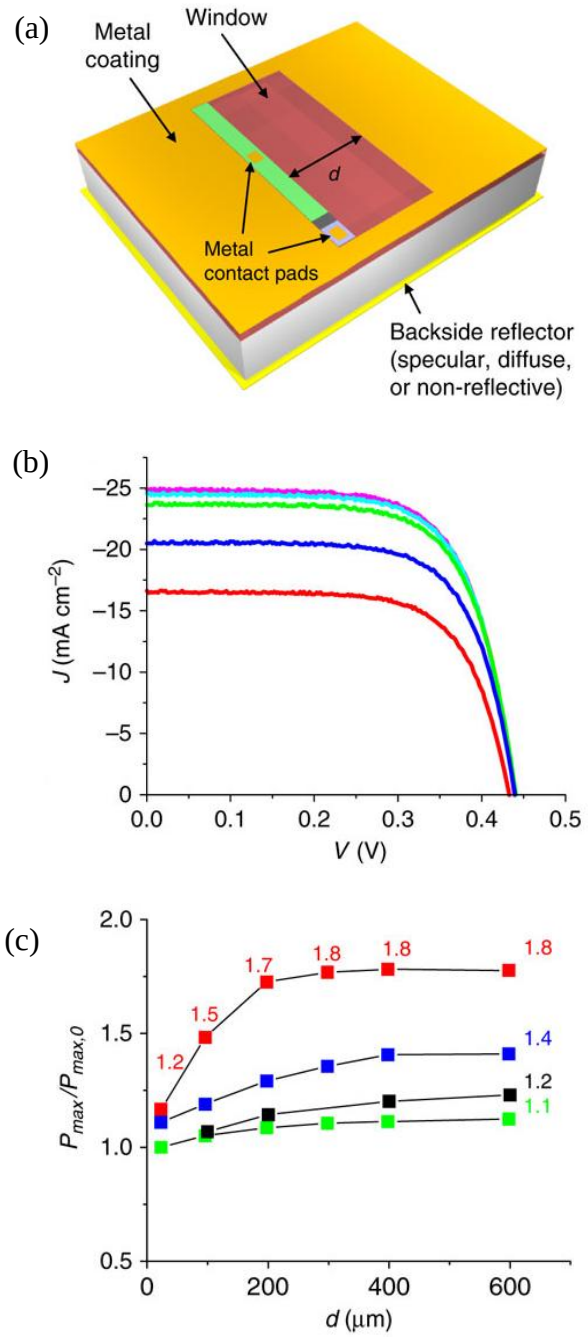



Figure 16. (a) Illustration of the model experiment. (b) J-V curves of cells as a function of aperture width, d, with a specular BSR (d=23 (red), 96 (blue), 200 (green), 300 (cyan), 400 (pink), 600 (orange) μm) (c) Normalized maximum output power ($P_{max}/P_{max,0}$) as a function of d and different systems – non-reflective (green), diffuse BSR with no DCM (black), diffuse BSR with DCM (blue), specular BSR with DCM (red). [25]

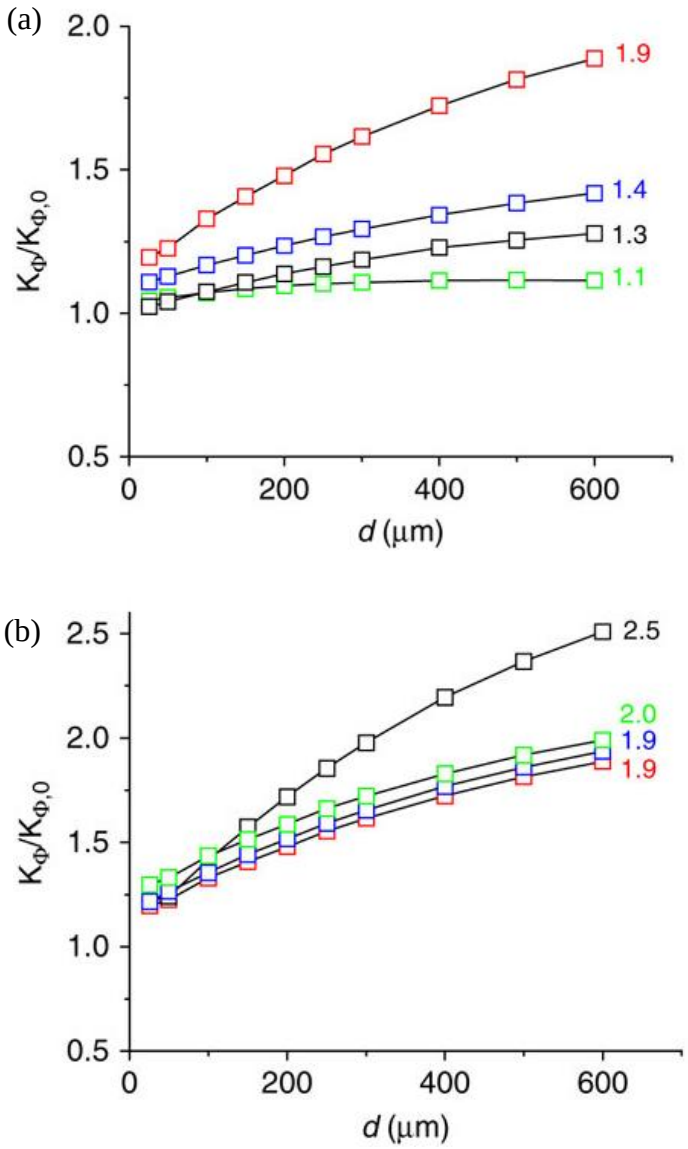



Figure 17. (a) Integrated total photon flux ($K_\Phi/K_{\Phi,0}$) as a function of d, with non-reflective (green), specular- (red) and diffuse-reflective (blue) BSRs. Data for the system without the DCM, with a diffuse-reflective BSR ,are also shown (black). (f) Integrated total photon flux ($K_\Phi/K_{\Phi,0}$) with specular reflective BSR, where various loss conditions are separately eliminated : non-TIR (black), self-absorption (blue) and imperfect BSR (green). A baseline (red) with all losses included is also shown. [25]

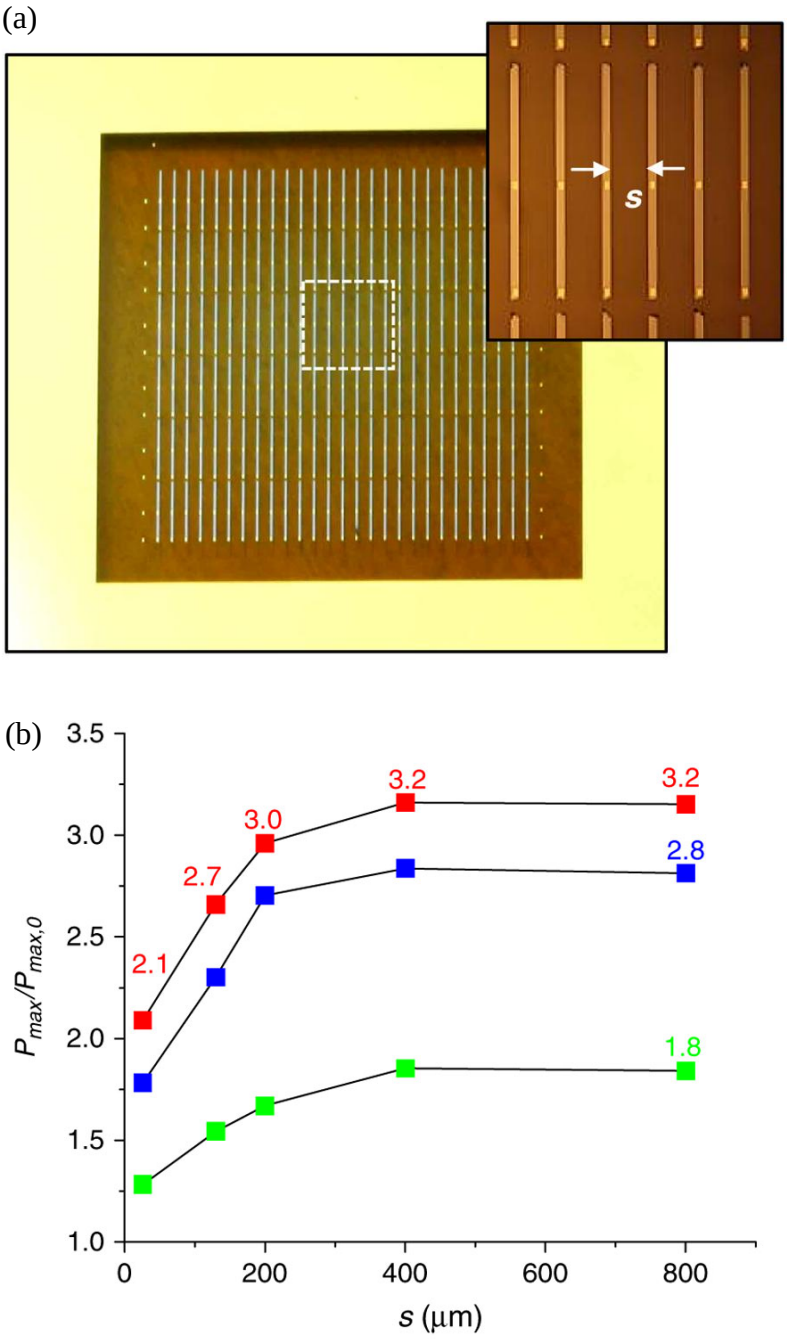



Figure 18. (a) Optical image of system with optimum spacing s = 400μm. (b) Normalized maximum output power ($P_{max}/P_{max,0}$) as a function of s with non-reflective (green), diffuse BSR with DCM (blue), specular BSR with DCM (red). [25]

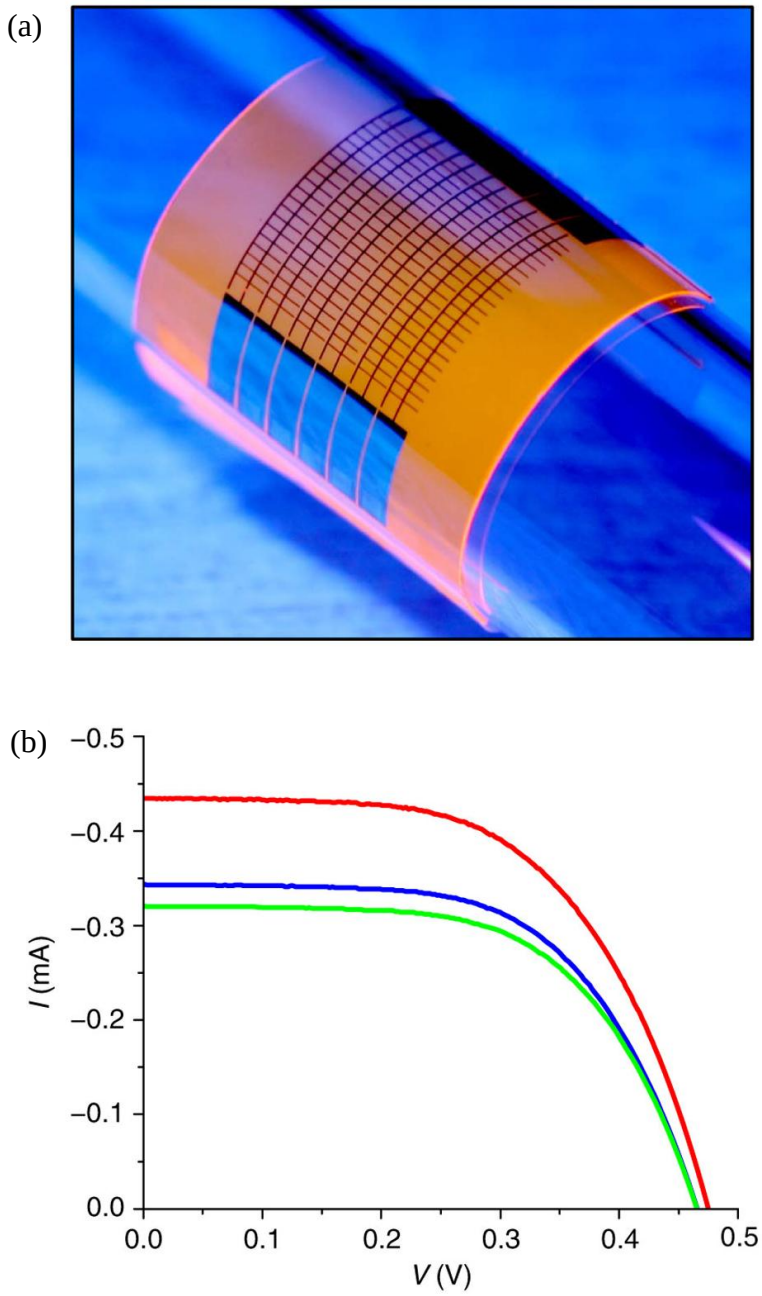



Figure 19. (a) Image of a representative device bent on a cylindrical support. Each metal grid line interconnects 21 μ-cells, with cell-to-cell spacings of 400 μm. (b) I-V curve (under AM 1.5D illumination) in flat (red) and bent states (bending radii of 6.0 mm (blue) and 4.5 mm (green)). [25]

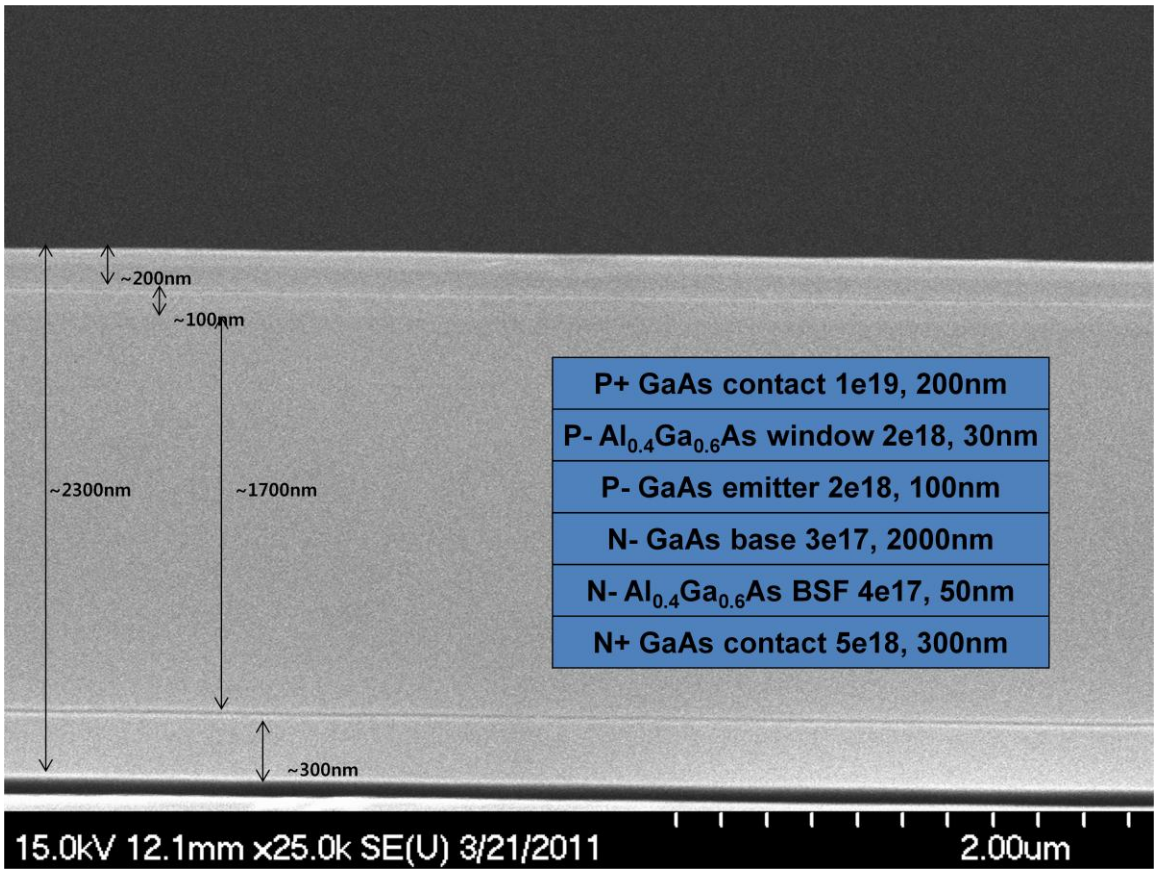



Figure 20. Cross-sectional SEM image of GaAs wafer and details of GaAs stack design.

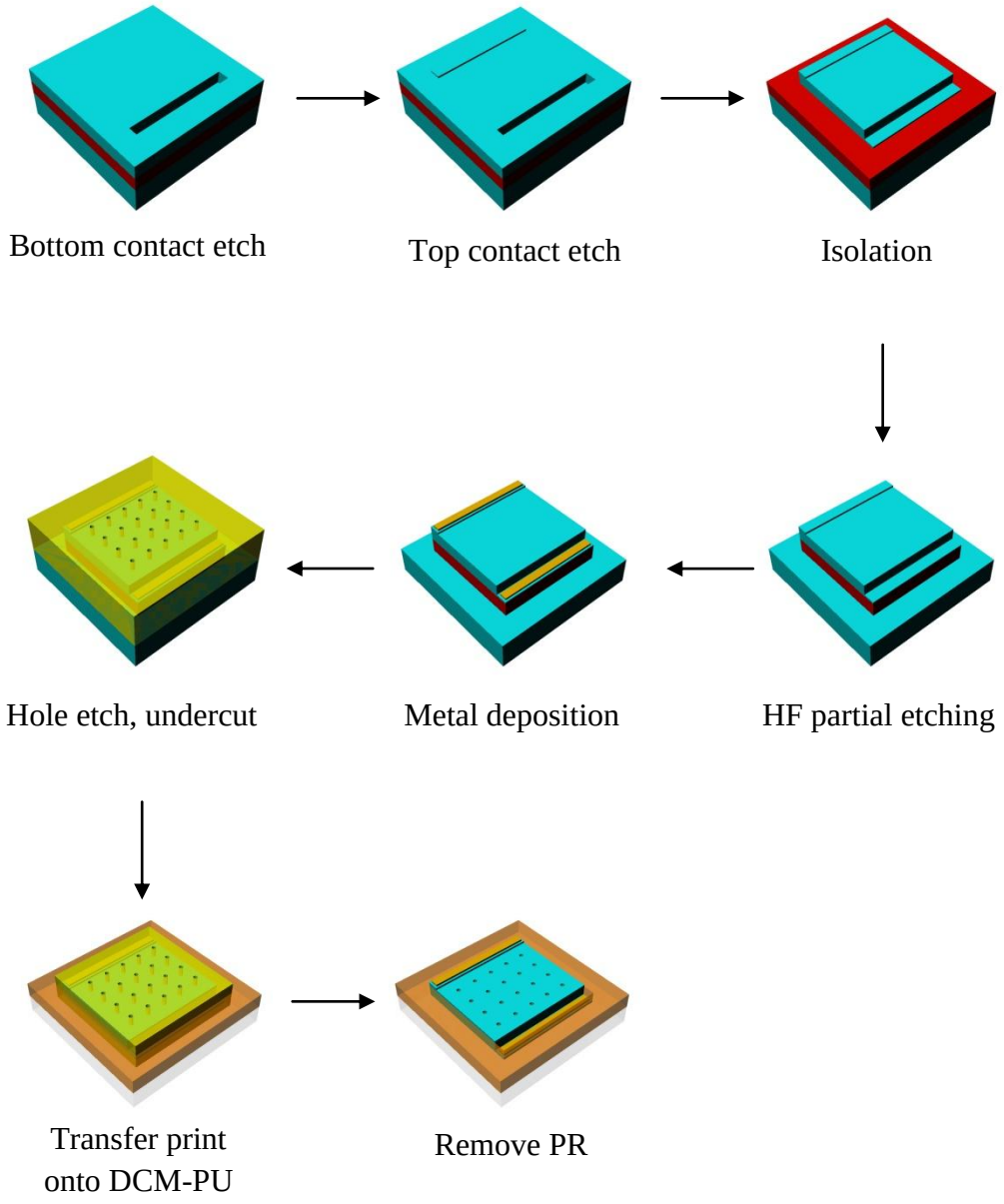



Figure 21. Schematic illustration of the fabrication process for the GaAs luminescent solar concentrator.

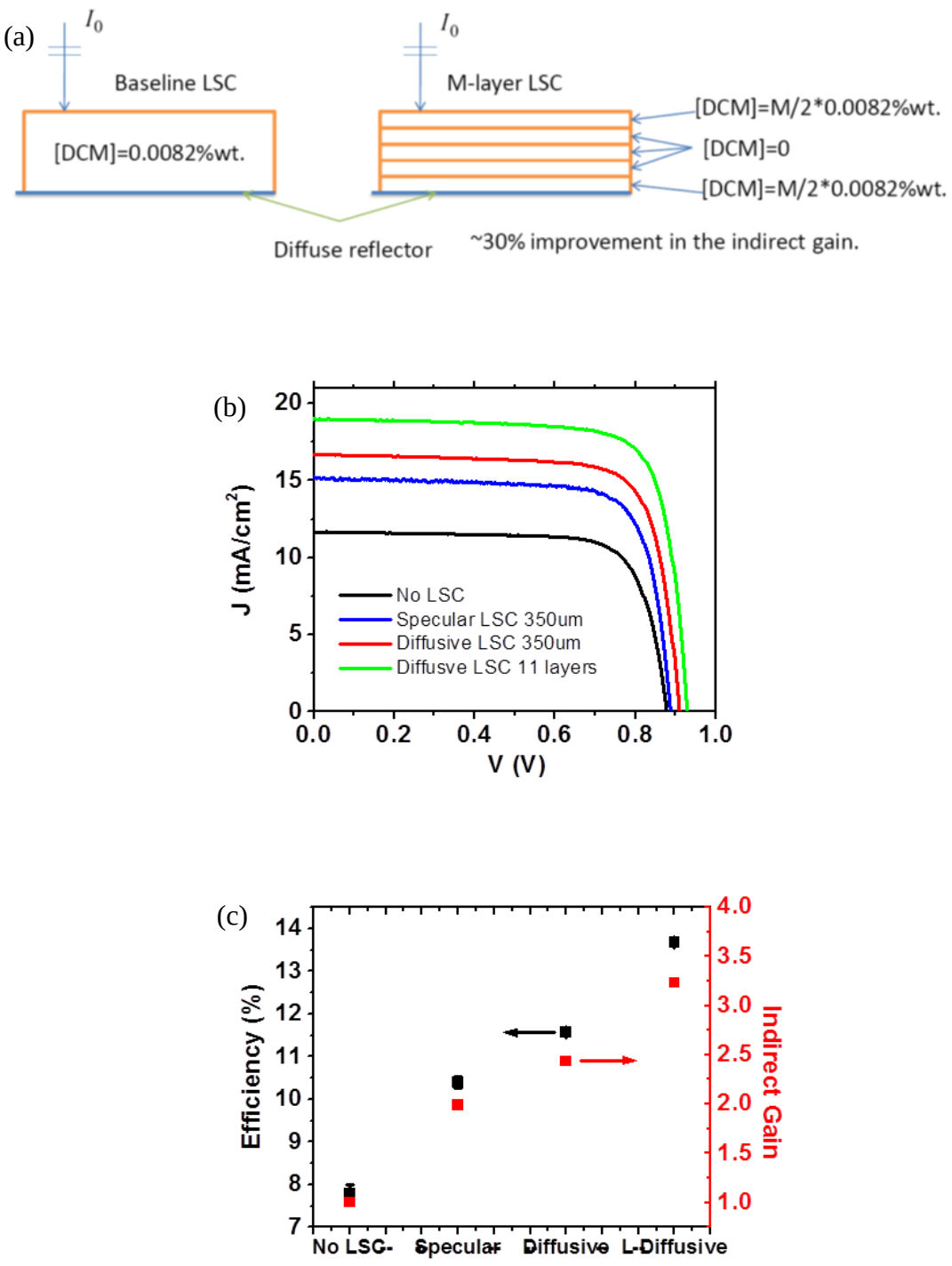



Figure 22. (a) Illustration of the multilayered DCM structure, (b) J-V curves for different types of LSC structures, (c) Efficiency and indirect gain for different BSR and structures.

# CHAPTER 4

# CONCLUSION

As the level of interest towards solar energy in growing, many new materials and methods are being developed. While these new materials are interesting and worth researching, there are still ways to exploit “old” materials such as crystalline Si or GaAs in a way that can overcome its limitations. This thesis discussed a method of utilizing Si in a way that i) reduces the material use and cost through transfer printing techniques and light trapping structures, ii) allow light weight, mechanically flexible designs, iii) enables user-definable transparency for interesting applications such as solar windows. Also it describes a new way of utilizing monocrystalline semiconductor materials and organic dyes for luminescent solar concentrators that i) reduces cost by using less semiconductor materials, and not requiring lenses and trackers for concentration, ii) works well for both direct and indirect illumination, iii) can be used for applications that require mechanical flexibility. The optics of the system and new structures for the LSC and BSR layers are currently being studied through the GaAs system.

# REFERENCES

[1] “Solar Energy Perspectives: Executive Summary”. International Energy Agency. 2011.

[2] Green, M. A., et al., “Solar cell efficiency tables (Version 38),” Progress in Photovoltaics: Research and Applications, 19: 565–572., 2011.

[3] Nelson. J., “The Physics of Solar Cells,” Imperial College Press, 2003.

[4] Green, M. A., "Solar cell fill factors: General graph and empirical expressions", Solid-State Electronics, vol. 24, issue 8, pp. 788 - 789, 1981

[5] Yablonovich, E., et al., “Intensity Enhancement in Textured Optical Sheets for Solar Cells,” IEEE Transactions on Electron Devices, vol. ED-29, pp. 300-305, 1982.

[6] Fossum, J. G., “Physical operation of back-surface-field silicon solar cells,” IEEE Transactions on Electron Devices, vol. 24, no. 4, pp. 322 - 325, 04/1977.

[7] Mack. S., et al., “Mechanically flexible thin-film transistors that use ultrathin ribbons of silicon derived from bulk wafers,” Applied Physics Letters, vol. 88, 213101, 2006.

[8] Hull, R. (ed.) “Properties of Crystalline Silicon,” The Institution of Electrical Engineers (IEE), 1999.

[9] Budianu, E., et al., Semiconductor Conf. 2002. CAS 2002 Proc. Int.Vol. 1 Institute of Electrical and Electronics Engineers (IEEE), 2002.

[10] Yoon, J., et al., “Ultrathin Silicon Solar Microcells for Semitransparent, Mechanically Flexible and Microconcentrator Module Designs,” Nature Materials 7, 907-915, 2008.

[11] Mousazadeh, H. et al., “A review of principle and sun-tracking methods for maximizing solar systems output.” Renew. Sust. Energy Rev. 13, 1800–1818, 2009.

[12] Luque, A. et al., “Concentrator Photovoltaics,” Springer, 2010.

[13] Weber, W. H. & Lambe, J., “Luminescent greenhouse collector for solar radiation.” Appl. Opt. 15, 2299–2300, 1976.

[14] Batchelder, J. S., et al., “Luminescent solar concentrators. 1. Theory of operation and techniques for performance evaluation.” Appl. Opt. 18, 3090–3110, 1979.

[15] Batchelder, J. S., et al., “Luminescent solar concentrators. 2. Experimental and theoretical analysis of their possible efficiencies.” Appl. Opt. 20, 3733–3754, 1981.

[16] Sansregret, J., et al., “Light transport in planar luminescent solar concentrators-the role of DCM self-absorption.” Appl. Opt. 22, 573–577, 1983.

[17] Barnham, K., et al., “Quantum-dot concentrator and thermodynamic model for the global redshift.” Appl. Phys. Lett. 76, 1197–1199, 2000.

[18] Gallagher, S. J., et al., “Quantum dot solar concentrators: electrical conversion efficiencies and comparative concentrating factors of fabricated devices.” Sol. Energy 81, 813–821, 2007.

[19] Bett, A. W., et al., “III–V compounds for solar cell applications.” Appl. Phys. A 69, 119–129, 1999.

[20] Bosi, M., et al.,“The potential of III–V semiconductors as terrestrial photovoltaic devices.” Prog. Photovolt. 15, 51–68, 2007.

[21] “Gallium Arsenide Solar cells”, Photovoltaic Systems Research & Development , Sandia National laboratories, 2002. Web. Dec. 2011. <http://photovoltaics.sandia.gov/docs/PVFSCGallium_Arsenide_Solar_Cells.htm >.

[22] Yoon, J., et al., “GaAs Photovoltaics and Optoelectronics Using Releasable Multilayer Epitaxial Assemblies,” Nature 465, 329-333, 2010.

[23] Schermer, J., et al., “Photon confinement in high-efficiency, thin-film III V solar cells obtained by epitaxial lift-off,” Thin Solid Films, vol. 511-512, pp. 645-653, 2006.

[24] Shir, D., et al., “Performance of Ultrathin Silicon Solar Microcells with Nanostructures of Relief Formed by Soft Imprint Lithography for Broad Band Absorption Enhancement,” Nano Letters 10, 3041–3046, 2010.

[25] Yoon, J., et al., “Flexible Concentrator Photovoltaics Based on Microscale Silicon Solar Cells Embedded In Luminescent Waveguides,” Nature Communications 2(343) DOI: 10.1038/ncomms1318, 2011.